IDENTIFYING CIRCUMSTELLAR DUST AROUND OXYGEN-RICH MIRA VARIABLES WITH MASER EMISSION VIA CONTINUUM ELIMINATION

A Dissertation

presented to

the Faculty of the Graduate School at the

University of Missouri-Columbia

In Partial Fulfillment

of the Requirements for the Degree

Doctor of Philosophy

---

by

LISA SHEPARD

Dr. Angela Speck, Dissertation Supervisor

JULY 2021

The undersigned, appointed by the dean of the Graduate School, have examined the dissertation entitled

IDENTIFYING CIRCUMSTELLAR DUST
AROUND OXYGEN-RICH MIRA
VARIABLES WITH MASER EMISSION VIA
CONTINUUM ELIMINATION

presented by Lisa Shepard,

a candidate for the degree of doctor of philosophy,

and hereby certify that, in their opinion, it is worthy of acceptance.

Professor Angela Speck

Professor Linda Godwin

Professor Sergei Kopeikin

Professor Haojing Yan

Professor Jacob McFarland

For my grandma, Gladys, who taught me that life is for living. I only recently learned what that really means. For Kelvin, Alexander, Juliet, and Dmitri, who are my stars.

ACKNOWLEDGEMENTS

I would like to thank and express my sincerest gratitude to my advisor, Dr. Angela Speck, who guided and mentored me through graduate school and life. I could not have done it without her.

My heartfelt appreciation goes to Dr. Linda Godwin for the conversations and advice. It has been a great pleasure to know her.

Special thanks go to the research group members I have worked with over the years. They taught me several little things which added up to a great experience. I also learned more when I had the opportunity to teach others. If I had not looked deeper into another student's radiative transfer modeling, I would never have fallen down the maser rabbit hole.

TABLE OF CONTENTS

LIST OF FIGURES

LIST OF TABLES

ABSTRACT

Stars between about 0.8 and 8 times the mass of the Sun will eventually evolve, becoming asymptotic giant branch (AGB) stars, where they pulsate and eject mass from their atmospheres, forming dust shells in the space around them. Evolved low- and intermediate-mass stars with carbon-to-oxygen ratios (C/O) below unity are known as oxygen-rich stars. O-rich stars are surrounded by dust shells containing mineral species dominated by silicate dust grains. In this dissertation, I examine whether dust grains around evolved, oxygen-rich AGB stars have any correlation with maser emission, and to understand the connection, if any, between specific types of maser emission and dust spectral features. I have investigated several methods of continuum elimination using spectroscopy data for the archetypal dusty AGB star, Mira. I have investigated the ~10μm and ~18μm spectral features in the continuum-eliminated spectrum including peak position, barycenter, and full width half maxima (FWHM). The positions and widths of observed spectral features were compared with those seen in laboratory spectra. I then looked for a correlation between maser emission and dust spectral features in a sample of Mira variables. The types of masers have been identified, and peak positions, barycenter positions, and FWHM have been measured for the sample spectra. The results show that the method of continuum elimination matters for correct identification of dust minerals, while varying the temperature and precise continuum shapes do not have a major effect on the positions of spectral features. Observed astronomical silicate features are complex and indicate the need for different compositions of minerals. Finally, there does not appear to be a correlation between the presence of a maser and dust spectral features based on the information available for analysis.

Chapter 1: Introduction

At the beginning of the Universe, all matter was in the form of hydrogen and helium; all elements heavier than helium form via nuclear fusion in stars. Newly-formed elements are ejected from stars either explosively (in the case of supernovae) or more gently over a few hundred thousand years for lower mass stars like the Sun. These new elements then become part of the interstellar medium (ISM), from which new stars and their planets form. The type of stars that produce most of the dust complement for the Galaxy start their lives as low- and intermediate-mass stars (0.8–8 $M_{\odot}$). Up to 95% of stars are low- and intermediate-mass (Kwok 2004). Dust forms around these stars during their second red giant phase, or Asymptotic Giant Branch (AGB) phase.

Dust is a vital ingredient in understanding many astrophysical environments. It plays an essential role in star formation processes and contributes to several aspects of interstellar processes, such as gas heating and the formation of molecules (e.g., Videen & Kocifaj 2002; Draine 2003; Krishna-Swamy 2005; Krugel 2008). In addition, since mass-loss from evolved stars is radiation-driven, it is intimately linked to the precise nature of circumstellar dust, which affects the coupling between stellar radiation and circumstellar material (Woitke 2006). Dust needs to be well understood in its own right if we are to understand how it contributes to many aspects of astrophysics.

We can study the dust around low- and intermediate-mass stars both during the formation phase and in the subsequent phases of stellar evolution as the circumstellar material is slowly dispersed into the ISM. AGB stars are major contributors of cosmic dust to the interstellar medium. A majority of AGB stars are known to have maser

emission. Since maser emission is associated with energy and density of molecules around a star, it is expected that the presence of an astrophysical maser is related to what type of dust forms in an AGB star's circumstellar dust shell.

The goal of this dissertation is to determine whether dust grains around evolved, oxygen-rich AGB stars have any correlation with maser emission, and to understand the connection, if any, between specific types of maser emission and dust spectral features.

The first project consisted of investigating several methods of continuum elimination to verify whether removing the continuum affects the shape, strength, and position of the spectral features. Using high-resolution space-based spectroscopy data along with ancillary data from the published literature, I identify dust grains around the archetypal dusty star, Mira. This is achieved by matching the positions and widths of observed spectral features with those seen in laboratory spectra. To do this comparison properly, it is necessary to account for the continuum emission in the observed spectra. I have investigated several methods of continuum elimination to determine whether the analysis is robust.

The second project investigates the formation of circumstellar dust by using a sample of oxygen-rich Mira variables for which maser emission has been identified. Using high-resolution spectroscopy data along with ancillary data from the published literature, I explored a relationship between the presence of maser emission and dust spectral features for the sample of Mira variables. I have investigated these spectra via continuum elimination by first matching the positions and widths of observed spectral features with those seen in laboratory spectra and then determining whether trends exist between the maser emission and dust spectral features.

Since the dust formation, processing, and dispersal is intimately linked to the evolution of AGB stars, we need to discuss how these stars evolve, and it is necessary to provide some introduction to these stars. In the next chapter, I will provide some relevant background about AGB stars followed by a chapter regarding dust and laboratory spectra to provide context for the work on identifying dust features. In Chapter 4, I will discuss masers and maser emission to set the stage for relating dust and masers. Chapters 5 and 6 contain the continuum-elimination study and maser study, respectively. Conclusions and future work are in Chapter 7.

Chapter 2: Asymptotic Giant Branch Stars

2.1. Evolution of Low- and Intermediate-Mass Stars

In the late stages of evolution, low- and intermediate-mass stars (0.8–8$M_{\odot}$; LIMS). follow a path on the H-R diagram up the AGB (Iben & Renzini 1983). During the AGB phase, these stars are very luminous ($\sim 10^3 - 10^4\,L_{\odot}$) and large ($\sim$300 $R_{\odot}$) but have relatively low surface temperatures ($\sim$3000 K). AGB stars pulsate due to dynamical instabilities, leading to intensive mass loss and the formation of a circumstellar shell of gas. As the gaseous material drifts away from the star, it cools and molecules can form, followed by the formation of small particles (dust grains), leading to a circumstellar envelope of dust and gas. The dust grains tap into the tremendous luminosity power of the star and drive a radiation-pressured wind (e.g., Hofner & Dorfi 1997). This wind causes AGB stars to lose mass at such tremendous rates (10^{-6}–$10^{-4}\,M_{\odot}\,yr^{-1}$) that they wither into white dwarfs rather than explode as supernovae (Iben & Renzini 1983; Vassiliadis & Wood 1993; Blocker & Schonberner 1991).

Mass loss increases during the AGB phase and, thus, the dust shells get thicker (both optically and geometrically; see Fig. 2.1), and these stars eventually become invisible at optical wavelengths and very bright in the infrared (IR). At this stage, intense mass loss depletes the remaining hydrogen in the star's outer envelope and terminates the AGB phase. The rapid depletion of material from the outer envelope of the star means that this extremely high mass-loss phase must have a relatively short duration (a few $\times 10^4$ years; Volk et al. 2000). During their ascent of the AGB, these stars also evolve chemically, starting with oxygen-rich atmospheres. Helium burning forms ^{12}C, which is

dredged up to the stellar surface by strong convection currents in the mantle. Thus, carbon is injected into the stellar atmosphere. The stability of the CO molecule in the stellar atmosphere means that the carbon-to-oxygen ratio (C/O) controls the chemistry around the star: whichever element is less abundant will be entirely locked into CO molecules, leaving the more abundant element to control dust formation. Therefore, AGB stars can be either oxygen-rich or carbon-rich. For the O-rich AGB stars, C/O can vary from approximately cosmic (C/O ≈ 0.4) to just less than unity. Once C/O is greater than unity these stars become C-rich (occurring in stars with masses ~2-4 $M_{\odot}$). Other nuclear processes also occur in the He- and H-burning shells of AGB stars and thus other new elements are also dredged up and enrich the dust formation region.

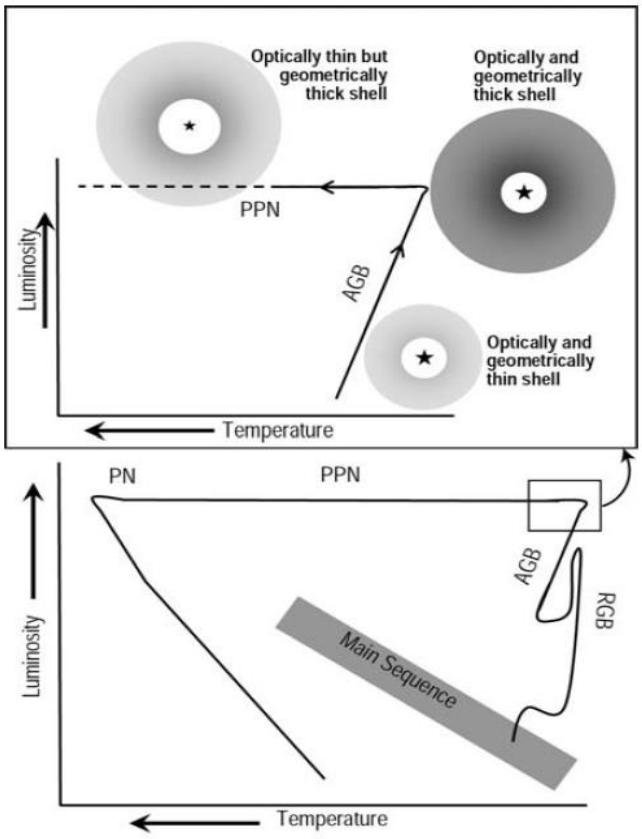

Figure 2.1: Schematic H-R diagram showing post-main-sequence evolution of LIMS. RGB = Red Giant Branch; AGB = Asymptotic Giant Branch; PPN = pre- or proto-planetary nebula; PN = planetary nebula; upper panel shows close up on AGB and PPN phases and cartoons the changes in dust shell densities.

2.2. Pulsation Mechanism

Normally, stars are stable and exist in a state of hydrostatic equilibrium. The inward gravitational force on the star's mass is balanced by the outward force of pressure exerted by the solar gas. The equation of hydrostatic equilibrium is:

$$\frac{dP(r)}{dr} = -\rho(r)\left(\frac{GM(r)}{r^2}\right) \qquad (2.1)$$

G is the universal gravitation constant. The pressure P, density ρ, and mass m are all functions of the radius of the star, r. Normally, a star will adjust itself if a small imbalance between the two sides occurs. If the star begins to contract, its internal temperature and pressure will increase and reverse the contraction. If the star begins to expand, its internal pressure and temperature will decrease, and gravity will restore matter to the original state. Friction also helps to maintain the balance by dissipating energy of motion (Percy 2007).

The derivation of the equation of hydrostatic equilibrium assumes that the forces acting on any element of material are exactly balanced. At times, this will be incorrect; a star undergoes periods of radial expansion and contraction during its lifetime, and sometimes the departure from equality will grow and the star will become unstable (Tayler 1996). The equation can be generalized as:

$$\rho(r)a = \frac{GM(r)\rho(r)}{r^2} + \frac{\delta P(r,t)}{\delta r} \qquad (2.2)$$

a is the acceleration of the inward radial direction, and the partial derivative with respect to radius is used because pressure is now a function of both radius and time. Instabilities in a star will be found automatically when the generalized equation is used (Tayler 1996).

For a star to start and maintain pulsation, some mechanism must convert radiant energy to kinetic energy that overcomes friction. Pulsating stars possess photometric or spectroscopic variations due to generally periodic physical changes, such as a change of stellar radius and surface temperature (LeBlanc 2010). Each type of variably pulsating star is found on a specific region of the Hertzsprung-Russell Diagram. This suggests that light variation is not an accident but a phenomenon that requires a very specific combination of physical conditions. Temperature is an important factor for the instabilities required for pulsation.

Pulsation occurs due to the ionization of helium. All but the highest-temperature stars contain neutral helium in the photosphere. Deeper, where the temperature reaches 25,000-30,000 K, is the zone where helium can be singularly ionized (HeII). Doubly ionized helium, HeIII, occurs at about 35,000-50,000 K (Gautschy & Saio 1996). More luminous stars are larger and therefore have lower density in the outer regions, and ionization can occur at lower temperature when free electrons have more space (Percy 2007). For pulsation to occur, the stellar gas must have high opacity. This opacity is due to the ionization zone of HeII→HeIII (LeBlanc 2010). Before total ionization occurs, the energy levels of the helium atoms become increasingly occupied, and this hinders energy flow via radiative transfer. This results in a temperature increase below the HeII→HeIII ionization zone, which in turn increases the pressure and thrusts out the layers above it. This expansion uses energy and the gas cools. After the ionization zone reaches lower-temperature layers, the HeIII ions recombine with free electrons. The HeII ions become less excited and the opacity decreases, allowing the accumulated heat to dissipate. This

leads to a contracting phase, and the pulsation cycle repeats. This process is illustrated in Figure 2.2.

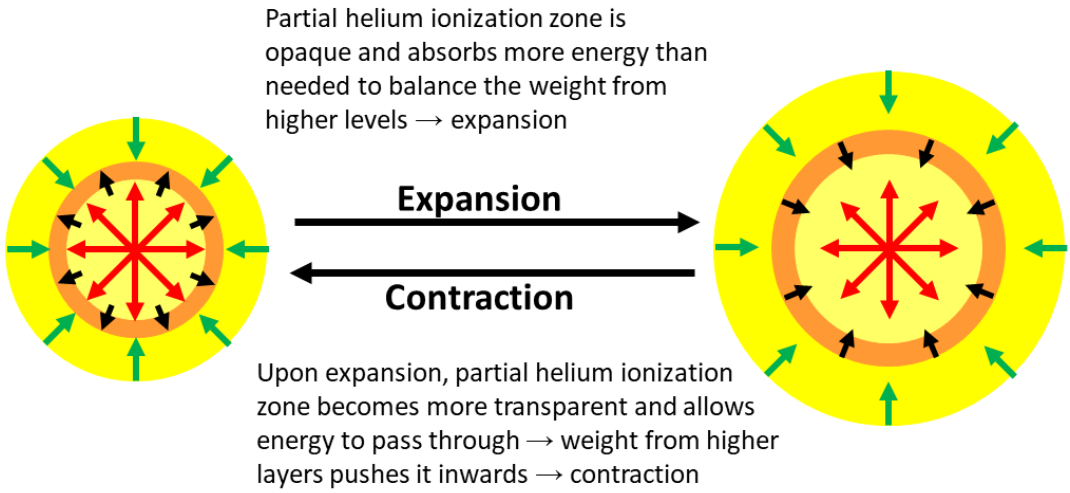

Figure 2.2: The pulsation mechanism.

The pulsation leads to mass loss through a dust-driven wind as described in §2.1. The shock waves produced by stellar pulsation lead to a dense, cool, extended stellar atmosphere, allowing for efficient dust formation. The dust formed in the outflow is dependent on the temperature, the mass-loss rate, and the elemental abundances in the stellar atmosphere. Mineralogy and dust formation is discussed in greater detail in Chapter 3.

2.3. Mira Variables

Mira variables are luminous red giant stars which fall in the category of Long-Period Variable (LPV). Pulsations periods range 100-1000 days, with most stars falling in the range of 150-450 days. The masses of Miras can be 0.8 to a few times the mass of the Sun with radii up to several hundred times the radius of the Sun. The period-luminosity

relation for Mira variables depends on the radius first and the mass second (Feast 1996). Compared to other types of variable stars, these giant stars have the largest pulsation amplitude; meanwhile, their visual brightness changes by more than 2.5 magnitudes, and for some, up to 10 magnitudes.

Their large size and brightness mean that there are more Miras known than any other type of variable star (see the *General Catalogue of Variable Stars* by Samus et al. 2017 and the AAVSO International Variable Star Index VSZ by Watson et al. 2014). This makes them ideal candidates for studies requiring a significant sample of similar stars.

Chapter 3: Mineralogy and Dust

3.1. Mineralogy

We have learned a great deal about the origin, nature, and consequence of cosmic dust since the discovery of silicates in space over 50 years ago. (Gillett et al. 1968; Woolf and Ney 1969). Typically, the mineralogy (the composition and crystal structure) of dust grains in space (astromineralogy) is studied by means of infrared (IR) spectroscopy. The IR is particularly suitable for this since the dust in a circumstellar envelope absorbs the light from the central star and re-radiates it at IR wavelengths. Dust particles of a given size, shape, temperature, structure, and composition, have their own signature IR spectrum (Woolf 1973). We can thus use the IR spectra of candidate dust species studied in the laboratory to identify IR spectral features observed in astronomical environments. Astromineralogy is a rapidly developing field and relies on laboratory studies of cosmic dust analogs.

The major factors in determining the mineralogy and size of the dust grains are the chemistry, density, and temperature of the gas from which it forms (Sharp & Wasserburg 1995). The chemistry determines the type of atoms available to form dust particles, whereas the density determines how likely these atoms are to come into contact and make dust particles (Bode 1988). The temperature determines which solid-state materials will be stable. The chemistry and density of a dust-forming circumstellar shell are in turn determined by the nature of the central star, including its metallicity and its initial mass, and by the evolution of the star. Stellar changes may lead to a transformation in the nature of the dust that is produced, which may in turn influence stellar evolution,

indicating a feedback relationship between the changes in the star and dust formation in its circumstellar envelope. For instance, if mass loss is radiation driven, the opacity of the dust grains affects the force of the radiation and thus mass-loss rate. Opacity is determined by the mineralogy and size/shape of the dust grains.

The classic "10μm" silicate feature was first observed in the late 1960s in the IR spectra of several M-type giants and red supergiants (RSGs; Gillett et al. 1968). Shortly thereafter, a 10μm absorption feature was discovered in the interstellar medium (ISM; Knacke et al. 1969; Hackwell et al. 1970). Since then, it has been found to be almost ubiquitous, occurring in many astrophysical environments including the solar system and extrasolar planetary systems (e.g., Mann et al. 2006, and references therein), the circumstellar regions of both young stellar objects (YSOs) and evolved intermediate-mass stars (AGB stars and planetary nebulae; e.g., Speck et al. 2000; Casassus et al. 2001), many lines of sight through the ISM in our own galaxy (e.g., Chiar et al. 2007), and in nearby and distant galaxies (e.g., Hao et al. 2005).

The silicate feature varies from location to location and temporally. Those variations have been attributed to optical depth and/or grain size effects, but in recent decades it has become clear that the culprit is most likely composition and structure of the silicate itself (see Speck et al. 2011 and references therein).

3.2. Brief Guide to the Structure of Silicate

Silicates are made up of SiO_4 tetrahedra. SiO_4 tetrahedron can be linked in a framework with each oxygen shared between two tetrahedra (e.g., SiO_2 minerals and feldspars), or they can be linked in chains (e.g., pyroxenes such as diopside [$CaMgSi_2O_6$]

or enstatite [$MgSiO_3$]), or they can be isolated tetrahedra (e.g., the olivines series: forsterite [Mg_2SiO_4] to fayalite [Fe_2SiO_4]). In all cases, the non-shared oxygens are charge-balanced by other cations (e.g., Mg^{2+}, Fe^{2+}, Ca^{2+}, Na^{2+}, etc.). The Ca-Mg-Al silicates that are expected to form in circumstellar environments are dominantly of pyroxene and olivine composition (Speck et al. 2011). How they are connected and what elements are included in the structure determine the type of silicate and thus its spectral features. Figures 3.1 and 3.2 illustrate the structures of olivine, melilite, and pyroxene.

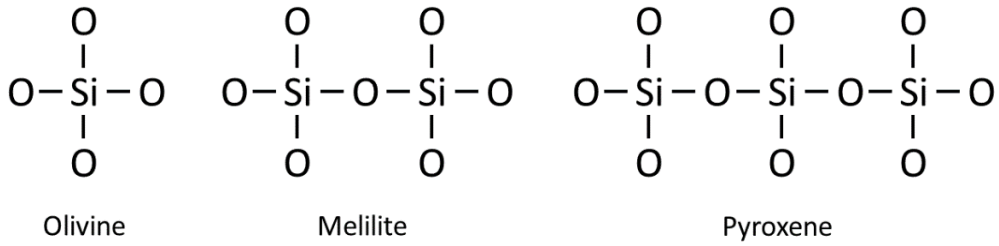

Figure 3.1: Schematic structures of the silicates olivine, melilite, and pyroxene.

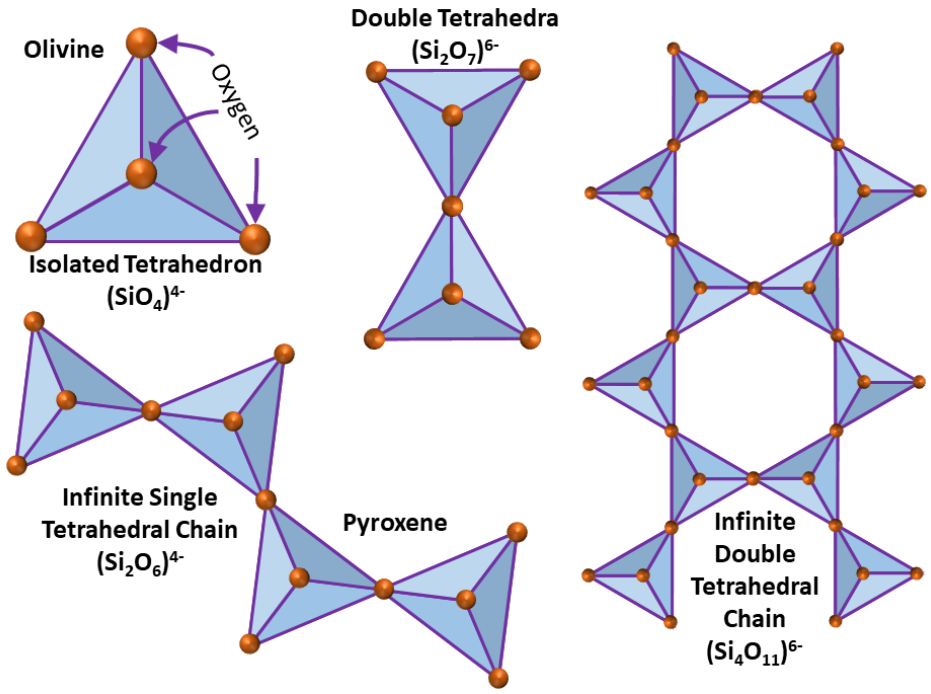

Figure 3.2: Three-dimensional models of silicates.

Different silicates will form at different pressures and temperatures, so being able to identify the precise type of dust gives us a diagnostic for what is happening in the dust-forming regions. Aluminum is a fairly abundant element in oxygen-rich stars. Thermodynamic studies (Tielens et al. 1997; Grossman 1972) predict that dust formation for the Al condensation sequence starts with the formation of crystalline Al_2O_3 (corundum or crystalline alumina) at about 1760 K. When the corundum cools, is reacts with gaseous SiO, Ca, and Mg to form melilite, first in the form of pure gehlenite ($Ca_2Al_2SiO_7$), later to transform partially into akermanite ($Ca_2MgSi_2O_7$) around 1550 K, corundum (above 1510 K), and spinel ($MgAl_2O_4$) below 1510 K. At about 1450 K, melilite reacts to form diopside ($CaMgSiO_6$) and spinel. The latter two have the possibility to transform into anorthite ($CaAl_2Si_2O_8$) through solid-solid reactions.

Only a small fraction of the Mg and Si is involved in this part of the condensation sequence. The main silicon-bearing minerals are formed through a separate condensation sequence. Most of the silicon nucleates and condenses first at about 1440 K as forsterite (Mg_2SiO_4). The excess SiO will eventually convert forsterite into enstatite ($MgSiO_3$) at about 1350 K. It is not very clear what happens with Fe in the described scenarios. Metallic iron is likely to be formed, but iron could also transform enstatite into forsterite and fayalite (Fe_2SiO_4) at 1100 K.

3.3. P-T Space and Dust Formation

The composition of AGB star dust depends upon pressure and temperature (P-T) in the dust-formation zone around the star. The precise astrominerals that can form

depend on various parameters, most notably C/O ratio and gas pressure (Lodders and Fegley 1999; Gail and Sedlmayr 1999). Gas pressure is a measure of the mass-loss rate ($\dot{M}$) convolved with the photospheric temperature ($T_{\odot}$) and outflow velocity (v_{exp}). Detailed calculations of the outflow structure (and its temporal variations) require the stellar temperature, radius, and luminosity. Applying the method from Speck et al. (2008, 2009) we can estimate the P–T space around a mass-losing star and compare with theoretical models for dust compositions forming under various P–T conditions. For a star with a mass-loss rate $\dot{M}$ and an expansion velocity of v_{exp}, the density ρ of the circumstellar shell at a radius r is given by:

$$\rho = \frac{\dot{M}}{4\pi r^2 v_{exp}} \qquad (3.1)$$

If we know the temperature and luminosity of the star and the composition of the outflowing material, we can combine this information with the Ideal Gas Law and a $T(r) \propto 1 / \sqrt{r}$ temperature distribution to determine the gas pressure at the condensation radius, which is the distance from the star where the gas has the condensation temperature.

For simplicity, the solid and gas phases are assumed to be at the same temperature. While this is clearly a simplification (Chigai and Yamamoto 2003), the temperature difference is small compared to the difference needed to significantly affect dust formation. We assume that most of the outflowing material is atomic hydrogen. In fact, it will probably be a mixture of atomic and molecular hydrogen (H_2) since H_2 forms around 2000 K and the temperature in the outflow is decreasing from the stellar surface temperature of ~3000 K to the dust condensation temperature in the 1000–1800 K range. An entirely molecular hydrogen gas would halve the gas pressure compared to the atomic

gas. However, we also assume an outflow velocity of 10 km/s, which reflects the speed of the outflowing material after radiation pressure acceleration. Adopting the pre-dust-formation outflow speed ($\lesssim$ 5 km/s) would increase the pressure. Thus, we can estimate where dust condensation zones fall in P–T space as a function of mass-loss rate, as shown in Figure 3.3.

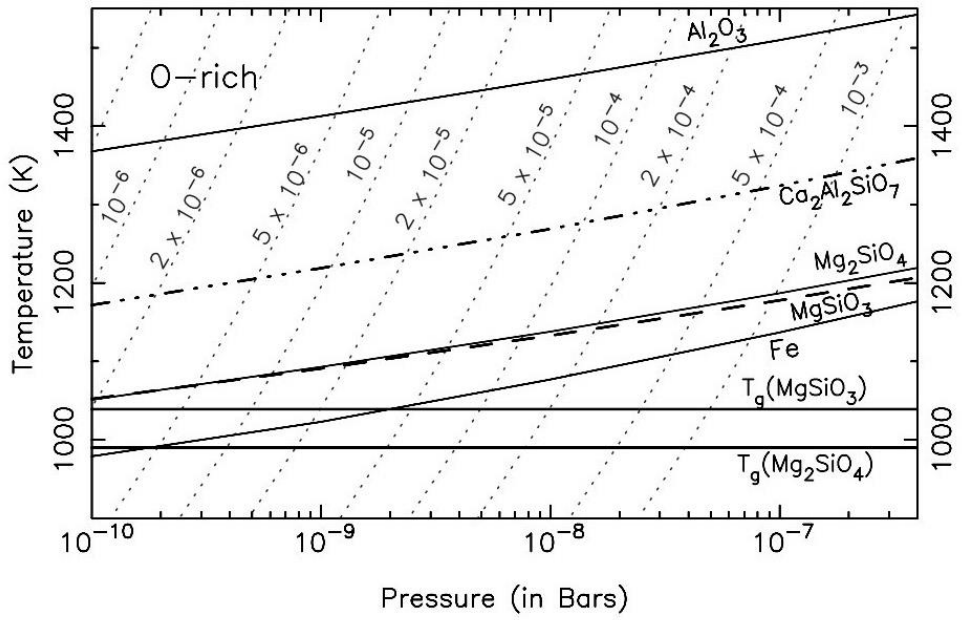

Figure 3.3: Pressure-temperature space in dust-condensation zone around O-rich AGB stars. *x*-axis is outflow gas pressure in bars, *y*-axis is outflow gas temperature in Kelvin. Solid and dashed lines indicate $T_{\rm dust}$ for a given pressure from thermodynamic equilibrium calculations (relevant compositions are labeled; from Lodders and Fegley 1995, 1999). For all $\dot{M}$ values, Al_2O_3 forms at a significantly higher temperature than the silicates, and thus can form a seed nucleus. Light grey dotted lines indicate the P–T paths for the outflowing gas for a range of $\dot{M}$ (indicated in $M_\odot$/yr) as calculated from Equation 3.1 and described above. Thick dark grey horizontal lines indicate glass transition temperatures (T_g) for Mg_2SiO_4 and $MgSiO_3$.

The ability to determine the type of dust that forms in astrophysical environments provides a diagnostic of the physical parameters therein. In the following chapters, we will use the information provided here to determine what sort of dust forms around maser-bearing AGB stars.

Chapter 4: Astrophysical Masers

4.1. Introduction to Lasers and Masers

If an atom absorbs a photon, an electron orbiting that atom will go to a higher energy state. Electrons do not stay at higher energy levels and will decay to a lower energy level, emitting a photon in the process. If this occurs without an external influence it is known as spontaneous emission. Usually, the number of atoms in a medium having a lower energy state will be greater than the number of atoms having a higher energy state. Under certain conditions, the reverse will be true, and the medium is described as having population inversion. Population inversion is required for lasers to work. The acronym LASER stands for "Light Amplification by the Stimulated Emission of Radiation". Stimulated emission occurs when a photon having a certain wavelength is fired at an atom that is already in an excited state. The atom absorbs the photon and quickly emits two photons of that wavelength as it decays to a lower energy level.

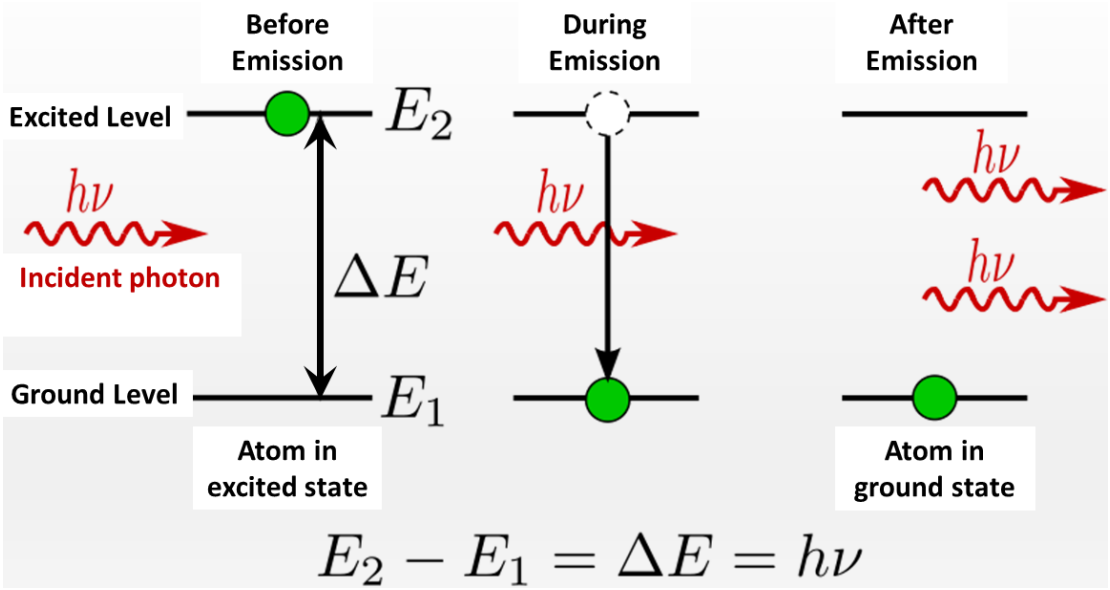

Figure 4.1: Schematic diagram of stimulated emission.

Lasers require a gain medium to amplify the light. Usually it is a gas, but it can be any state of matter which is put into an excited state by an external energy source. Sometimes it is possible to have lasing action with only a single pass of radiation through the gain medium. Usually, a resonant cavity is required to achieve lasing action, but it is not necessary for a laser to work. The excited molecules are funneled into a resonant cavity and emit photons through stimulated emission. Gain or amplification is exponentially related to the length of the resonant cavity. Most of the photons in a laser are reflected inside the cavity. If the resonant cavity is composed of mirrors on the ends, one of the mirrors is partially transparent so that the light can escape. Laser light is also notable because it is coherent. The emitted beam is monochromatic, stays collimated over a long distance, and maintains uniform polarization (Seigman 1986).

A maser is a laser that operates at microwave wavelengths. The acronym MASER is generally understood to stand for "Microwave Amplification by the Stimulated Emission of Radiation," although Charles Townes proposed that it stand for "Molecule" since it is the energy states of molecules that usually provide the transition for masing (Townes 1964). The first operational microwave amplifier was made in 1953 by Townes and his graduate students based on a theoretical paper written in 1951 by Joseph Weber. At that time, masers were not thought to be a natural occurrence. The first functioning optical laser was not made until 1960 and was initially called an "optical maser".

4.2. Laboratory Masers vs. Astrophysical Masers

An astrophysical maser is a region of gas which amplifies microwave radiation through stimulated emission. They can exist in molecular clouds, comets, supernova remnants, stellar and planetary atmospheres, and in distant galaxies. In astrophysical

masers, there is no resonance cavity. The radiation enters from a source and travels through the gain medium (usually molecular gas in which population inversion has occurred) in a single pass. Like laboratory masers, the emitted radiation is stimulated and monochromatic. However, the radiation from astrophysical masers is not spatially coherent. Radiation from natural masers can be very weak and difficult to detect due to the sensitivity of equipment and the spectra of surrounding molecules.

If we have maser emission, there must be a population inversion in the source, so that light amplifies through it. Maintenance of the inversion requires a pumping mechanism. Three types of mechanisms can contribute to the overall pump: collisions with partner atoms and molecules, which, in astrophysics, usually means a mixture of atomic and molecular hydrogen plus helium; radiation, usually of far-infrared (FIR) wavelengths (e.g., FIR photons excite the ground rotational states of OH molecules); and chemical reactions, which, when forming the maser molecule, leave it in the upper state of a maser transition (Gray 1999).

Population inversion is required for an astrophysical maser to occur, but other conditions are also necessary. There must be velocity coherence along the line of sight so that Doppler shifting does not prevent inverted states in different parts of the gain medium. Polarization can be attained in laboratory masers by selecting the desired modes, but polarization in natural masers depends on the pumping mechanism or the presence of a magnetic field (Strelnitski 1997).

While there is no resonant cavity, the gain or amplification is still exponentially related to the length traveled by the radiation through the gain medium. Since the maser cloud is not uniform in shape, there will be pathlength variations along different

directions. This has a significant effect on the output radiation. Beaming in an astrophysical maser will be greatest where the path length is greatest. Parts of the cloud will appear brighter than others. Any variation in conditions along the path will have exponential changes in the output. Emission lines will appear much narrower and taller than unamplified lines because the gain amplifies the center of the line shapes more than the edges. The emission brightness of a maser is such that a blackbody temperature would be much higher than the maser's actual temperature in order to have such intense output for the maser's wavelength (Strelnitski 1997). Astrophysical masers are often highly polarized due to magnetic effects (Gray & Field 1994). This can be up to 100% for circular polarization and is less for linear polarization (Garcia-Barreto et al. 1988). The polarization allows for conclusion to be made about the direction and strength of the magnetic fields, however the directions of ordered magnetic fields are similar to the field in the larger volume surrounding the masers (Fish et al. 2003).

4.3. Discovery

The first astrophysical maser was detected in 1965 (Weaver et al.). Before then it was believed that molecules could not exist in space, so when emission lines were discovered at a frequency of 1665 MHz, the responsible substance was named "mysterium". Soon after, the spectral line was identified as a transition of the OH (hydroxyl) molecule (Weinreb et al. 1965). An explanation of the signal as a natural microwave laser was given by Davies et al. in 1967. More maser transitions in more molecules were found: H_2O in 1969 (Cheung et al.), CH_3OH in 1971 (Barrett et al.), and SiO in 1971 (Wilson et al.). These maser discoveries were all found in molecular clouds. Masers were also discovered around highly evolved late type stars: OH in 1968 (Wilson

& Barrett), H_2O in 1969 (Knowles et al.), and SiO in 1974 (Snyder & Buhl). Masers were discovered in external galaxies in 1973 (Whiteoak & Gardner), and since then have also been seen in our solar system in comets.

The current list of astrophysical maser molecules includes:

- OH (hydroxyl)
- H_2O (water)
- CH (methylidyne)
- H_2CO (formaldehyde)
- NH_3 (ammonia)
- CH_3OH (methanol)
- SiS (silicon monosulfide)
- HC_3N (cyanoacetylene)
- SiO (silicon monoxide)
- HCN (hydrogen cyanide)
- H (hydrogen)
- CO_2 (carbon dioxide)

Typically, each molecule produces maser emission from more than one of its transitions, so the number of maser lines, or frequencies, which have been detected outnumbers the list of molecules many times.

4.4. Maser Environments

Most astrophysical masers are found in star-forming regions. These are composed of young stellar objects and HII regions embedded in molecular clouds. Typically, water, OH, and methanol masers are found in these environments. Excitation energy comes from radiation and collisions and results in maser emission of many transitions. The 6.7 and 12.2 GHz methanol masers had been recognized as excellent tracers of the physical conditions in massive star-forming regions, at scales from 1 to 1000 AU (1 milliarcsecond to 1 arcsecond at 1 kpc) (Batrla et al. 1987). Interferometric observations have shown that these masers arise within 3000 AU around the massive stellar object and that the masing regions have linear dimension from 1 to 100 AU.

Comets are small solar system bodies composed of frozen volatiles and tend to orbit the Sun in eccentric orbits. When the comets are near the Sun, the volatiles evaporate and form a halo and then a tail. In 1994, the comet Shoemaker-Levy 9 collided with Jupiter and a maser emission was observed in the 22 GHz region from water molecules (Cosmovici et al. 1995). Ultraviolet light from the Sun can break water molecules into OH molecules which can mase. In 1997, Comet Hale-Bopp was observed to have 1667 MHz maser emission from the OH molecules (Ogley et al.).

It is predicted that masers exist in the atmospheres of giant planets and stars. If so, such masers would be highly variable due to rotation. Water maser emission at 22 GHz was reported coming from Jupiter during the comet Shoemaker-Levy 9 collision, but also has been seen from several exoplanet host stars.

Another source type is from the interaction of supernova remnants (SNR) with dense molecular gas. A study by Green et. al (1997) found at least 33 detections of 1720 MHz maser transition of the OH molecule in a sample of 75 SNRs. Claussen et. al (1997) were able to observe SNR masers in many spots at the resolution of the Very Large Array (VLA) radio telescope. The observations had full polarization information and showed a weak magnetic field and a spot velocity spread of a few kilometers per second. There was some evidence that maximum amplification occurs when the acceleration due to the SNR shockwave is perpendicular to the direction of maser propagation.

Late-type stars support the action of a variety of masers at different distances from the star. Due to the pulsation of the star, there are periods of increased temperature, and the outflowing material produces shockwaves in the outer atmosphere. Silicon monoxide (SiO) masers can be produced at about 5-10 AU, Water masers at about 100-400 AU, and Hydroxyl masers at about 1000-10000 AU (Vlemmings et al. 2006). The radius of formation for these masers is dependent on whether conditions can support masing action for each species. Silicon Monoxide maser emission requires high temperatures (>1000 K) and densities ($>10^9$ cm^{-3}; Elitzur 1980). SiO masers form in large emission cells that form in the extended atmosphere, the region between the photosphere and the dust formation point (Elitzer 1992). The silicon monoxide gas condenses into dust at larger radii and is not available for masing action to occur. The boundaries for water masers depend on the density limits for maser operation. H_2O masers are of interest because they precisely trace the region of the circumstellar envelope, where condensation of dust and outward acceleration of the gas-dust mixture begins (Habing 1996). The main input of energy and momentum to gas in a circumstellar shell comes from friction with

dust particles driven through it by radiation pressure (Lewis 1998). The 22 GHz water maser occurs where the temperature ranges from 300 K to 100 K, and densities are 10^7-10^9 cm^{-3} (Benson & Little-Marenin 1996). At the far distances where hydroxyl masers are found, UV radiation dissociates water molecules (Gray 2012).

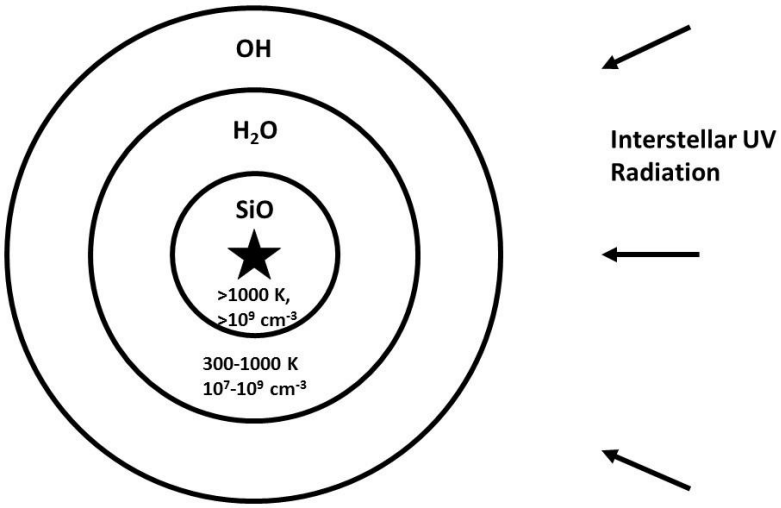

Figure 4.2: A schematic structure of maser shells. Silicon monoxide masers exist close to a star, where temperature and density are the greatest. Water masers can exist where temperature is low enough for molecules to exist in an excited state, yet density is high enough for gain. At further distances from the star, interstellar UV radiation can dissociate water molecules into hydroxyl.

Masers observed in distant galaxies usually have a different source type which is far more energetic. These "megamasers" have been observed around the active cores of certain external galaxies (Baan et al. 1982). These sources are typically a million times brighter than the maser sources in our galaxy. Hydroxyl, water, and formaldehyde masers have been observed, with water being the most powerful (Lo 2005). They are at least the

size of the solar system. Some megamasers form near the accretion disk around a black hole. Measuring maser velocity and centripetal acceleration spots allow for distance and mass to be accurately measured.

4.5. Conclusion

Masers reveal the composition, temperature, density, velocity, and magnetic field of certain regions of space. They tell us of the environments in different areas of space, from young stars, to comets, to super-massive black holes. Masers exist in specific environments, many of which were hypothesized to not exist naturally. They reveal certain areas invisible to regular telescopes, such as galactic centers, and allow the measurement of distances to other galaxies as well as their speed and direction. Since masers require very specific density and temperature to switch on, their observation at high resolution would reveal the nature of the physical conditions in a variety of astrophysical environments.

Chapter 5: The Effect of Continuum Elimination in Identifying Circumstellar Dust around Mira

5.1. Introduction

Asymptotic Giant Branch (AGB) stars are major contributors of cosmic dust to the interstellar medium; understanding their contribution to interstellar dust is essential to the broader topics of evolution and composition of stellar and interstellar objects in our universe. We identify dust grains in space by matching the positions of observed spectral features with those seen in laboratory spectra. While radiative transfer modeling should allow us to build a spectrum that includes all contributions to the observed spectra, we are hampered by a paucity of appropriate laboratory data for such modeling. Typically, we need the complex refractive indices of candidate minerals in order to perform radiative transfer modeling. While there are many simple absorption or transmission spectra measurements for candidate minerals, very few minerals have corresponding complex refractive indices. This limits the application of radiative transfer modeling if we want to determine the detailed mineralogy of the dust.

In some cases (usually very optically thin scenarios), we can simply eliminate a continuum contribution to the observed spectrum to isolate any observed features and measure their basic spectral parameters (peak and barycentric positions, relative strength, full width half maxima). In this project, I investigate several methods of continuum elimination to verify whether removing the continuum will affect the shape, strength, and position of the spectral features.

5.2. Background

5.2.1. Fitting the Continuum

To fit and remove the continuum from an observed spectrum, we need to consider what contributes to the photons we receive. As long as the dust shell is not very opaque (i.e., it its optical depth is low), an observed spectrum can be represented by

$$F_{tot} = F_*(\lambda) + F_{dust}(\lambda) \qquad (5.1)$$

Some starlight is always obscured by the dust, which is why this equation is most applicable to optically thin situations. As optical depth increases, more starlight is removed and significant radiative transfer occurs, making this simple equation no longer accurate.

We can then break down the light emitted by the dust, F_{dust} (dustlight) as follows:

$$F_\lambda = F_* + \sum_{i=1,j=1}^{n,m} C_j \times Q_{\lambda,j} \times B_{\lambda,i}(T_i) \qquad (5.2)$$

where each B_i represents a single dust temperature blackbody (of which there are n total), each $Q_{\lambda,\text{j}}$ represents the wavelength-dependent extinction efficiency for a single grain type as defined by its size, shape, composition, and crystal structure, and each C_j represents the scale factor for a single grain type (of which there are m total). This means that at each given wavelength the emission from the individual dust species is simply added to give the total emission at that wavelength. In cases where the dust shell is optically thick, the starlight will be significantly extinguished and simply subtracting the star is difficult.

It is possible to subtract the star's contribution to the spectrum by using either an observed spectrum of a naked star of similar temperature (like e.g., Sloan et al. 2003A) or by using a stellar atmosphere model (from e.g., Allard 2016). However, the precise details of the stellar spectrum, with all the molecular absorption features, especially those due to CO and SiO, are sensitive to the exact temperature and composition of the stellar atmosphere. The goal of this paper is not to accurately model the underlying star, but to assess the effects of the processes of deconstructing observed spectra of dusty stars on extracting data about the dust. Therefore, rather than applying a detailed model of the stellar atmosphere, we approximate the star as a black body with a temperature T_*. Subtracting the stellar flux F_* gives:

$$F_{dust} = \sum_{i=1,j=1}^{n,m} C_j \times Q_j \times B_i \qquad (5.3)$$

The spectrum is often simplified to:

$$F_\lambda = C \times Q_\lambda \times B_\lambda(T) \qquad (5.4)$$

where B_λ (T) is the Planck function for a blackbody of temperature T, Q_λ is a composite value including contributions from all dust grains of various sizes, shapes, crystallinities, and compositions, and C is a scale factor that depends on the number of dust particles, their geometric cross section, and the distance to the star. In the literature, this equation has been applied to the entire spectrum including the star; or it has been applied after subtraction of a stellar or blackbody spectrum. This project determines the sensitivity of the positions and shapes of spectral features to the simplification of the spectrum to Equations 5.1–5.4.

5.2.2. Previous Studies with Continuum Elimination

Different methodologies have been used to eliminate the continua from stellar spectra to extract dust spectral features that follow the theory described in §5.2.1. The usual techniques are continuum subtraction or division, but the choice of continuum shape also varies. The opacity (optical depth) of the dust shell should influence which method is used. As outlined in the previous section, if the circumstellar dust shell is optically thin, the blackbody spectrum of the star should be subtracted from the total flux to isolate the spectral features of the dust. An optically thick dust shell will be dominated by the spectrum of the dust which will obscure the flux coming from the star. While previous work using continuum elimination has covered many different types of dust environments, here we focus on previous work on O-rich Asymptotic Giant Branch (AGB) stars.

Previous work which used continuum elimination methods include Sylvester et al. (1999), Dijkstra et al. (2005), and Speck et al. (2008) who all used the continuum division method. Sylvester et al. (1999) used data from the Infrared Space Observatory (ISO) Short- and Long-Wavelength Spectrometers (SWS and LWS, respectively) to examine a sample of seven oxygen-rich AGB stars with dense (optically thick) circumstellar dust shells. In these OH/IR stars, the dust completely obscures the stars at visible wavelengths. Mira was also presented for comparison. Their method used a "pseudo-continuum" spline-fit to approximate the general shape of this continuum. Division by a spline fitted continuum was also employed by Dijkstra et al. (2005) who examined 7-14μm ISO spectra of a sample of 12 M-type evolved stars of varying mass-loss rates and therefore different optical depths. Both these papers use spline-fit

approaches, which does not necessarily correlate with a real, physical cause for the continuum. Speck et al. (2008) also applied a continuum-division method, focused on IRAS 17485-2534, a highly obscured oxygen-rich AGB star. In this case, the continuum was modeled as a 400K blackbody rather than a spline fit. The match of the observed continuum to a single blackbody temperature would suggest that we are seeing an isothermal surface within the dust shell. This represents the depth at which the shell becomes optically thick. The lack of extra emission at longer wavelengths suggests that any outlying dust is low enough in density to have an insignificant contribution to the overall emission (c.f. Speck et al. 2009).

There are many examples of previous studies which used continuum-subtraction to extract dust spectral features. Volk & Kwok (1987) examined Infrared Astronomical Satellite (IRAS) Low-resolution Spectrometer (LRS) 8-22μm spectra for a sample of 467 oxygen-rich AGB stars having a wide variety of optical depths. The continuum was fit with a power law of the form $F \propto \lambda^{\beta}$ on either side of the 10-μm feature. The power-law fit is taken to represent the true continuum over the feature, and the strength of the feature is measured relative to the continuum. Little-Marenin & Little (1988), used a similar method to study the dust emission seen in IRAS LRS spectra of 79 MS, S, and SC stars. In this case, they fit a blackbody energy distribution to both sides of an emission feature and subtracted this continuum from the observed spectrum. Little-Marenin & Little (1990) applied a slightly different continuum to a larger sample of (291) Mira variables observed with IRAS LRS. In this study, they subtracted a 2500 K blackbody from each observed spectrum prior to classifying the shape and position of the 10μm spectral feature. Sloan & Price (1995) also used IRAS LRS spectra to investigate a sample of

variable oxygen-rich AGB stars and the silicate emission at 10μm. They isolated dust emission by modeling the stellar continuum with a modified Planck function, fitting it to the spectra, and subtracting it. These studies all fit the star and subtracted it; they just approximated the star differently.

Following on from IRAS, researchers found new details in the spectra of cosmic dust from the ISO. While examining the 13μm dust emission feature in the ISO SWS spectra of optically-thin oxygen-rich circumstellar dust shells, Sloan et al. (2003A) eliminated the continua by fitting a naked (dust-free) oxygen-rich AGB star spectrum and subtracting it. The 131 stars in the sample are mostly AGB with some supergiants and objects transitioning between AGB and planetary nebula stages. Molster et al. (2002) used spectra from the ISO SWS and LWS to study a sample of 17 oxygen-rich circumstellar dust shells surrounding evolved stars, ranging from AGB stars to the planetary nebula phase and including some massive red supergiants and objects whose status is unclear. They used a spline fit to approximate the continuum, which they subtracted.

Speck et al. (2000) analyzed the ground-based (UKIRT) 8-13μm spectra of 142 M-type stars, including 80 oxygen-rich AGB stars and 62 red supergiants. The dust features in the 10μm region were examined using normalized, continuum-subtracted spectra. For each source, a 3000 K blackbody representing the stellar photosphere was normalized to the spectrum at 8.0μm. This was then subtracted from the observed astronomical spectrum. It is also worth noting that varying the assumed 3000 K blackbody temperature by +/- 1000 K had very little effect on the size and shape of the derived continuum-subtracted dust features, but the precise positions were not measured.

This is similar to the result found by DePew et al. (2006), where radiative transfer models showed that the stellar temperature does not have a major effect on positions and strengths of spectral features.

These different approaches have also been used to study various types of objects other than stars. Markwick-Kemper et al. (2007) looked at grain properties in the dust composition in a broad absorption line quasar observed with the Spitzer Space Telescope and used a power law to fit the continuum. The method included a continuum-divided spectrum, assuming the emission region is optically thin in the infrared. This is to yield the resulting opacity of the dust, and the temperature dependence has been eliminated by dividing the spectra by the continua. They also subtracted a spline-fit continuum of each spectrum to provide the same base line and ran models on the continuum-divided spectrum. Peeters et al. (2002) used ISO SWS spectra to fit continua for PAH bands using a sample of 57 sources including reflection nebulae, HII regions, YSOs, evolved stars, and galaxies. They used a variety of methods to extract the feature profiles including subtracting a local spine continuum, subtracting a polynomial of order 1, drawing a general continuum splined through chosen points, and drawing a continuum under features. It is worth noting that PAH spectral features are much narrower than the 10μm silicate feature, and this is less affected by difference in the choice of continuum.

Methods for eliminating the continuum have varied, and the effect of different methodologies has not been adequately explored. When working with an optically thick system, the star is hidden visibly, and one can divide a blackbody. This blackbody represents the dust temperature in the circumstellar shell where the medium transitions from optically thin to optically thick. Division by the blackbody extracts the dust

emission/absorption efficiencies (Q_λ) as given in Equation 5.4. When working with an optically thin system, simply subtracting a stellar continuum (F_*) leaves a residual dust spectrum (F_{dust}) that still depends on the dust temperature (see Equation 5.3). This temperature dependence has been largely neglected when measuring or classifying the residual dust spectral features. It should be noted that there are intermediate optical depths where significant radiative transfer occurs such that the simplification to either Equation 5.1 (optically thin) or Equation 5.4 (optically thick) is not applicable. In these cases, it is necessary to apply full radiative transfer modeling.

Next, we explore the effect of applying Equations 5.1-5.4 as different pathways to isolating and measuring observed dust features using the optically thin star, Mira.

5.3. Mira as a Case Study

Mira has the distinction of being the first known variable star, having been discovered over 400 years ago. This pulsating AGB star has a period of 332 days, a V-band magnitude ranging 2-10.1, and spectral type M5–9IIIe. The temperatures corresponding to Mira's spectral type range over 3420–2667 K (see the stellar spectral flux library by Pickles 1998). Mira itself exists as a binary system consisting of the AGB star (Mira A) and a compact accreting companion (Mira B), first seen optically in 1923 (Aitken). The classic 10μm silicate spectral feature was first observed in the late sixties in the infrared (IR) spectra of several M-type giants and red supergiants (RSGs) including Mira (Gillett et al. 1968).

This well-studied, archetypal, dusty star is used here to demonstrate that the analysis method affects the interpretation of dust spectral features and to find which

method(s) of continuum elimination should be applied to the analysis of similar AGB stars.

Many dusty stars have been classified according to their mid-infrared (IR) spectra obtained by the IRAS LRS. Mira has been classified by Sloan & Price (1998) as infrared emission class SE8, indicating silicate and oxygen-rich dust composition with classic narrow silicate emission. Kraemer et al. (2002) classified Mira as infrared spectral class 2.SEc, representing strong silicate emission features with peaks at 10-12μm and 18-20μm. Sloan et al. (2003A) extended this work and classified Mira as IR spectral class 2.SE8, signifying a lack of a 13μm feature. Speck et al. (2000) used UKIRT spectra to classify Mira's dust features as silicate AGB A, indicating a "classic" narrow 9.7μm silicate feature.

Mira displays the classic circumstellar 10μm silicate dust emission feature seen in many dusty environments. Understanding the nature of the silicate dust are important to so many astrophysical environments (e.g. Videen & Kocifaj 2002; Draine 2003; Krishna-Swamy 2005; Krugel 2008; Mann et al. 2006; Casassus et al. 2001; Chiar et al. 2007; Hao et al. 2005) but interpreting this classic spectral feature is sensitive to how we extract it from our observations. In the next section we will investigate this sensitivity.

5.4. Measuring the Spectral Parameters

Mira was observed using ISO SWS on February 9th, 1997. The fully processed post-pipeline spectral data were acquired from an online atlas associated with Sloan et al. (2003B). Detailed data reduction information is available from the atlas website, accessed at https://users.physics.unc.edu/ gcsloan/library/swsatlas/aot1.html. I acquired the

BVJHK photometric fluxes and the IRAS 12, 25, 60 and 100μm photometry data from the SIMBAD astronomical database[1]. I also retrieved the V-band magnitude from the AAVSO[2] database for the exact date of the ISO SWS observation. The resulting spectral energy distribution (SED) is shown in Figure 5.1.

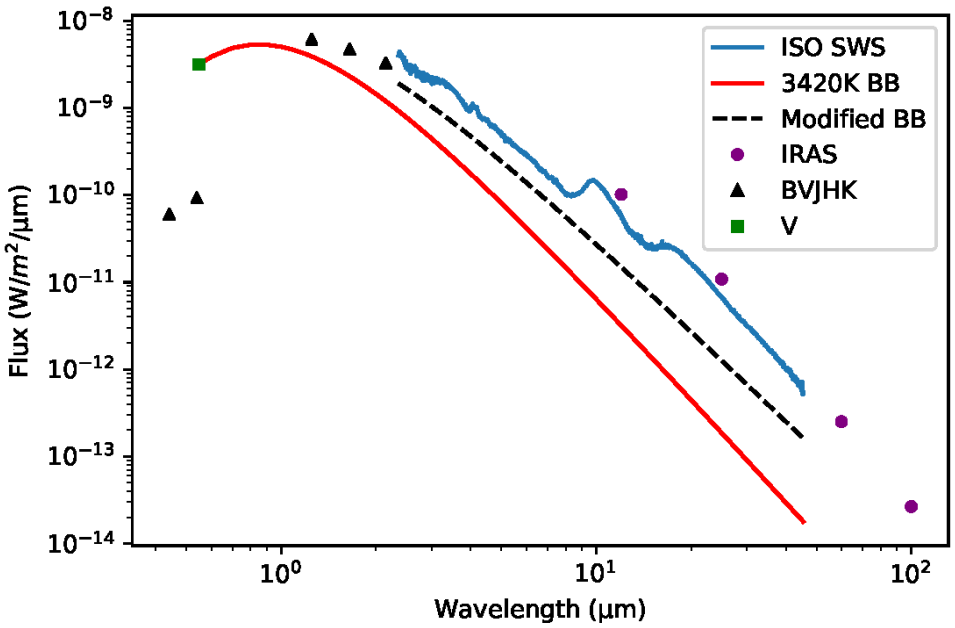

Figure 5.1: The spectral energy distribution for Mira together with the stellar blackbody spectrum (T = 3420 K) and the best fit modified blackbody. The black triangles are the flux values in the BVJHK bands; the purple dots are the flux values in the four IRAS photometry bands; the green square is the V-band flux for the same date as the ISO SWS observations; the blue line is the ISO SWS spectrum of Mira; the red line is a 3420 K blackbody fitted to the observed data at V-band; and the black dashed line is the best fit modified blackbody. x-axis is wavelength in μm and y-axis is flux density in $\mathrm{Wm^{-2}\mu m^{-1}}$.

1 http://simbad.u-strasbg.fr/simbad/

2 American Association of Variable Star Observers, https://www.aavso.org/

The lightcurve from AAVSO shows that the observation date for the ISO SWS spectrum is close to that of the maximum brightness of Mira (Figure 5.2), allowing us to constrain the stellar temperature to the highest value for known spectral range of Mira, i.e., 3420 K. The V-band photometric data point for the observation date was used to normalize our stellar (3420 K) blackbody to the SED as shown in Figure 5.1.

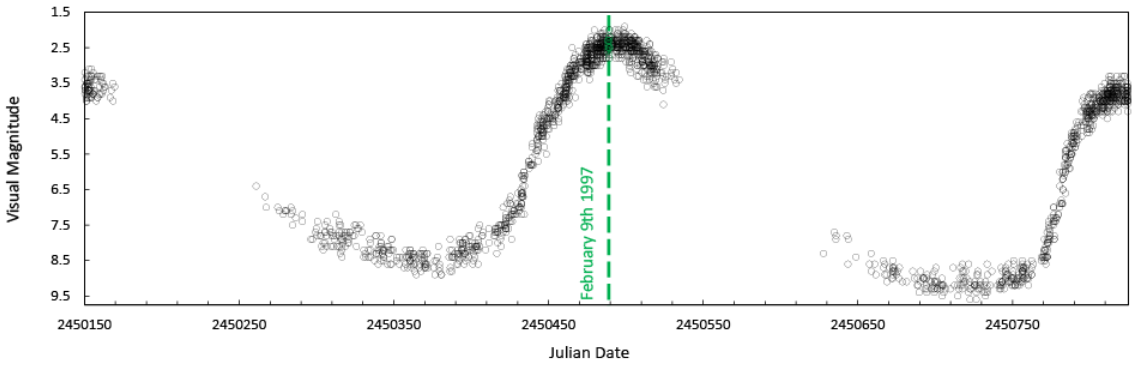

Figure 5.2: The V-band light curve for Mira over a 22-month period (2 full pulsation cycles) from AAVSO. The ISO SWS observation date is indicated by a green dashed straight line. The x-axis is Julian Date, and the y-axis is visual magnitude.

To determine the sensitivity of spectral feature measurements to the choice of continuum elimination, I used six pathways, which fall into two categories: 1) Fit and subtract a stellar blackbody; or 2) fold the stellar contribution in equation 1 into the overall dust flux as in Equation 5.4.

If we subtract a stellar continuum, we must then subtract or divide a dust continuum. If we subtract a continuum, we must then fit another dust continuum and divide by it. If we divide by the continuum, then we are left with some form of emission efficiency (Q-value). If we divide by the initial "stellar" continuum, we are assuming that Equation 5.4 applies, and we cannot make any more steps. We can only divide by a

continuum once! The list of pathways, along with symbols/abbreviations is summarized in Table 5.1 and a flow diagram to show each pathway is given in Figure 5.3.

Table 5.1: Definition of terms

Name/symbol	Definition
F_{tot}	the total flux coming from Mira and the surrounding circumstellar dust
F_{tot}/BB_{*}	total flux received divided by stellar blackbody
$F_{tot}/(BB/\lambda^{\beta})$	total flux received divided by a modified blackbody with emissivity index
F_{dust}	total dust flux = total flux received with stellar blackbody subtracted
$F_{dust}/(BB/\lambda^{\beta})$	total dust flux divided by a modified blackbody with emissivity index
F_{dust}-BB_{dust1}	total dust flux with a dust continuum subtracted
$(F_{dust}$-$BB_{dust1})/BB_{dust2}$	total dust flux, with a dust continuum subtracted and then divided by a second dust blackbody continuum.

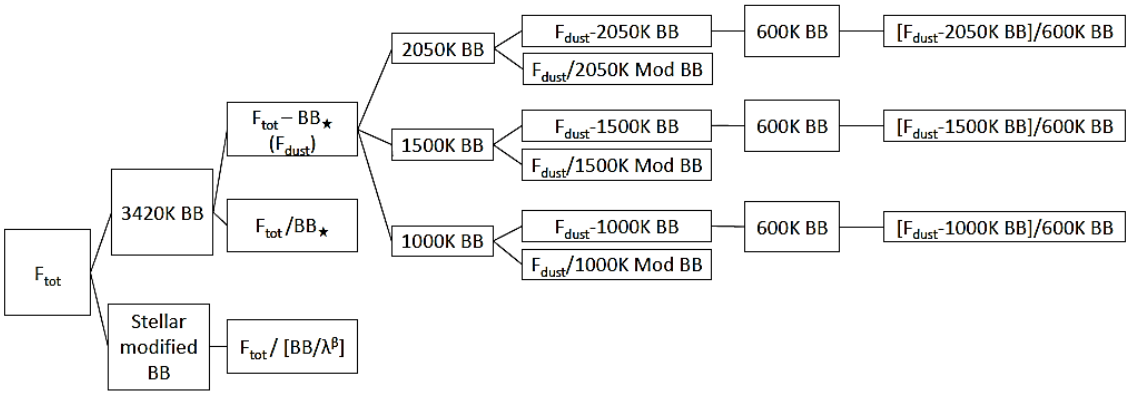

Figure 5.3: Continuum elimination pathways.

Following Equation 5.1, we can isolate the TOTAL emission from the dust by subtracting the stellar blackbody. The resulting dustlight spectrum (Fdust) is shown in Figure 5.4. Once we subtract the star, the next step is to fit the dust continuum with either a regular or a modified blackbody where the modified version can be expressed as BN =

$B\lambda^{-\beta}$, and β is the emissivity index for the dust. The dust continuum is then divided out to leave a continuum-eliminated spectrum (see e.g., Figure 5.5).

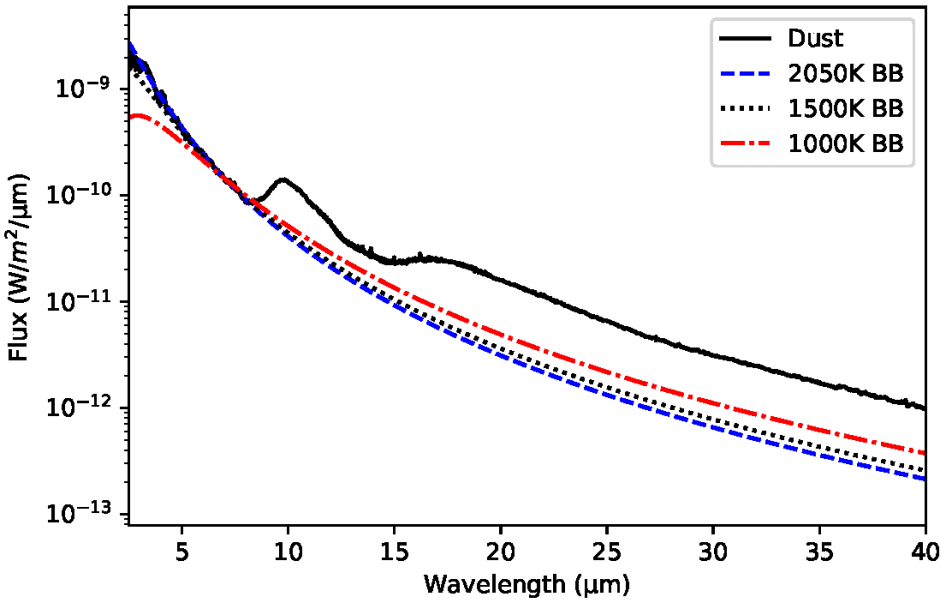

Figure 5.4: F_{dust} - the stellar-blackbody-subtracted or total dust spectrum for Mira together with the dust continuum blackbodies. The black line is F_{dust}; the dashed blue line is a 2050 K blackbody; the dotted black line is a 1500 K blackbody; and the dot-dash blue line is a 1000 K blackbody. The x-axis is the wavelength in μm and the y-axis is flux density in $Wm^{-2}\mu m^{-1}$.

I developed a program called MiraFitter which allows us to fit blackbodies (or modified blackbodies) to any spectrum. The original, flux calibrated ISO SWS data is $F_{tot} = F_* + F_{dust}$, the total flux from both the star and the dust surrounding it. As described in Section 5.2.1, stars with optically thin dust will need the stellar flux subtracted in order for us to examine the dust. To fit a blackbody, MiraFitter uses a Planck curve for a given temperature; we can select the wavelength at which Planck curve is normalized to the

observational spectral data. We can also apply a modification via an emissivity law (as described above, where β is the emissivity index).

In addition to fitting blackbodies and/or modified blackbodies, MiraFitter analyzes the spectral features in each of the continuum-eliminated spectra produced by following the 6 pathways shown in Figure 5.3 and Table 5.1 as well as in the original, total flux spectrum (F_{tot}). MiraFitter can find the peak position of the silicate emission features at 10μm and 18μm, calculate the barycentric positions of those features, and measure their full width half maxima (FWHM). While there is often an emphasis on the "peak position" for dust spectral features, both the peak and barycentric positions are important for discriminating between different potential astrominerals. The combination of the peak, barycenter, and FWHM gives a good measure of both the position and the shape of the spectral features. This will be discussed further below and in §5.6.

To identify the peak positions around ~10μm and ~18μm in all the various continuum-eliminated spectra, MiraFitter determines the maximum flux in the ranges 9.5–10.5μm and 17.6–18.3μm and then the corresponding wavelength of each peak. These positions were examined visually to ensure that the peak measurement is not due to a noisy point in the observed spectrum. This methodology is applied to seven different versions of the same original spectrum (as listed in Table 5.1).

The barycentric position of a dust spectral feature is often not aligned with the peak position (see e.g., Speck et al. 2011). While barycenter is often used in terms of the center of mass of a system, in spectroscopic terms, the barycenter of a spectral feature is the wavelength at which the energy within the feature is split exactly in half. Therefore, we need to calculate the area under the curve of the spectral feature and split that area in

half to find the centroid or barycenter. The barycentric positions of the ~10μm and ~18μm features as well as the FWHM for the ~10μm are listed in Table 5.2. The ~18μm peaks are not consistently defined, and FWHM values are not reported. It should be noted that many previous studies of dust features simply fit the continuum on either side of the silicate features at 10 and 18μm (e.g., Volk & Kwok 1987; Little-Marenin & Little 1988), which does not yield a clearly defined 18μm feature. But the application of this method will shift the position of the observed feature and make comparison to laboratory data difficult. This will be discussed further in §5.6.

Table 5.2: Spectral Feature Measurements

	peak position		barycenter		FWHM~10
	~10μm	~18μm	~10μm	~18μm	(μm)
F_{tot}	9.83	17.64	10.15	17.75	2.18
F_{tot}/BB_{*}	10.37	18.20	10.49	19.06	2.87
$F_{tot}/(BB/\lambda^{\beta})$	10.12	18.20	10.44	18.97	2.77
F_{dust}	9.83	17.64	10.16	17.74	2.05
1000 K $F_{dust}/(BB/\lambda^{\beta})$	9.83	18.20	10.36	18.83	2.36
1500 K $F_{dust}/(BB/\lambda^{\beta})$	9.83	18.20	10.39	18.86	2.47
2050 K $F_{dust}/(BB/\lambda^{\beta})$	9.83	18.20	10.40	18.88	2.54
1000 K $F_{dust} - BB_{dust1}$	9.83	17.64	10.20	18.27	2.36
1500 K $F_{dust} - BB_{dust1}$	9.83	17.64	10.19	18.20	2.34
2050 K $F_{dust} - BB_{dust1}$	9.83	17.64	10.19	18.16	2.34
1000 K $(F_{dust} - BB_{dust1})/BB_{dust2}$	9.83	18.20	10.37	18.93	2.70
1500 K $(F_{dust} - BB_{dust1})/BB_{dust2}$	9.83	18.20	10.37	18.93	2.76
2050 K $(F_{dust} - BB_{dust1})/BB_{dust2}$	9.83	18.20	10.37	18.93	2.76

As described in Section 5.2.1, Equation 4 has been applied to analyzing the whole spectrum including both dust and starlight. In this case, the version of the spectrum that is considered continuum eliminated is F_{tot}/BB_{*}, i.e., the total flux divided by the blackbody spectrum of the star. This is best applied when the system is optically thick and there is

little *direct* starlight to remove (e.g., Sylvester et al. 1999; Speck et al. 2009). More examples of work that have used this version of continuum elimination are given in Section 5.2.2. The F_{tot}/BB_* spectrum is shown in Figure 5, while the $F_{tot}/(BB/\lambda^{\beta})$ spectrum (divided by modified blackbody) is shown in Figure 6.

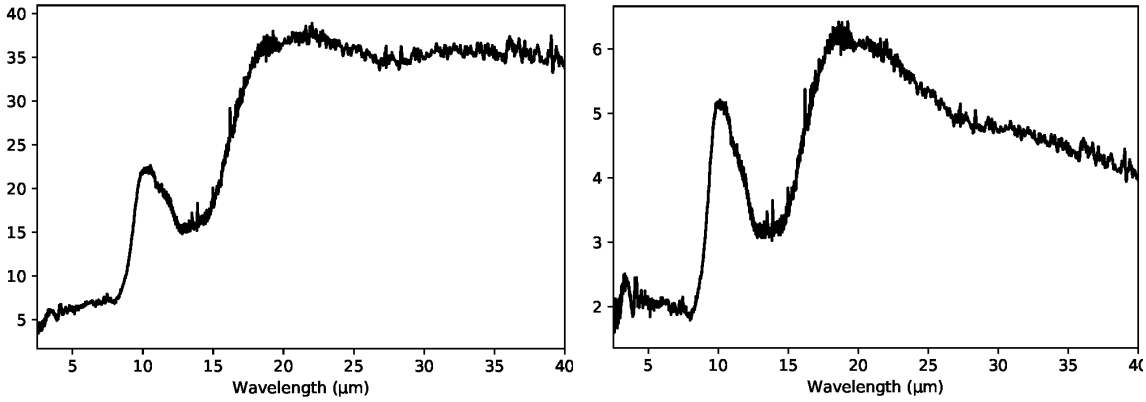

Figure 5.5 (left): The ISO SWS spectrum of Mira divided by 3420 K stellar blackbody. x-axis is wavelength in μm and the y-axis is normalized flux. Figure 5.6 (right): The ISO SWS spectrum of Mira divided by a modified blackbody. x-axis is wavelength in μm and the y-axis is normalized flux.

When the system is optically thin enough that there is a significant contribution to the total spectrum (F_{tot}) by *direct* starlight, we must subtract the stellar blackbody to isolate the emission from dust ($F_{dust} = F_{tot} - F_*$, see Equation 5.1). There is always some uncertainty in the stellar temperature, especially for variable stars. In many studies, AGB stars have been assumed to be 3000 K for simplicity. Mira itself has a range of temperatures from 2667 K to 3420 K. To determine whether the precise temperature of a stellar continuum affects the peak position of the spectral dust feature, I varied the stellar blackbody temperature. I found that temperatures ranging 2493 K and above could be

used before the peak positions around 10μm and 18μm are affected. The TOTAL dust spectrum (i.e., the stellar blackbody-subtracted spectrum) F_{dust} is plotted in Figure 5.4.

Applying a blackbody modified by an emissivity law (BB/λ^{β}) as the continuum may be appropriate, depending on the precise nature of the dust. The emissivity index, β, depends on the size, structure, composition, and temperature of the dust grains as well as the optical depth of the dust shell (e.g., Demyk et al. 2017, and references therein). While in reality β should have a value in the range 1-2 to have a physical meaning (Koike et al. 1987; Mennella et al. 1998), laboratory experiments have shown that it is possible to have emissivity indices outside this range (Koike et al. 1980, where amorphous carbon has a $\beta \approx 0.8$). Moreover, a negative β value can be used to mimic a continuum that is the sum of several blackbodies of differing temperatures. Figure 5.7 demonstrates that using a negative β value emulates the summing of several blackbodies of different temperatures into a single spectrum. In this case, the value of β reflects the range of temperatures and the total amount of dust at each temperature.

For fitting a modified blackbody to our Mira SED, the value of β was varied until the best fit (by eye) was achieved. This is established using a visual tool within MiraFitter that displays both the spectrum being fitting and the fitting modified blackbody as well as a plot of the resultant divided spectrum. The presence of both the silicate features and the numerous molecular absorption feature makes a chi-squared minimization difficult to apply, but the divided spectrum should be flattened (on average, ignoring the dust and molecular features). This fitting process yielded β = -0.5. This best-fitting modified blackbody is shown with the SED in Figure 5.1. A range of β values were tested to determine at what values the peak positions were affected. The $\sim$10 μm peak is

unchanged for -0.79 ≤ β ≤ -0.03, and the ~18 μm peak is unchanged for -1.99 ≤ β ≤ 0. It is notable that the beta value is always negative, indicative of a range of dust temperatures combining to give the continuum (see Figure 5.7).

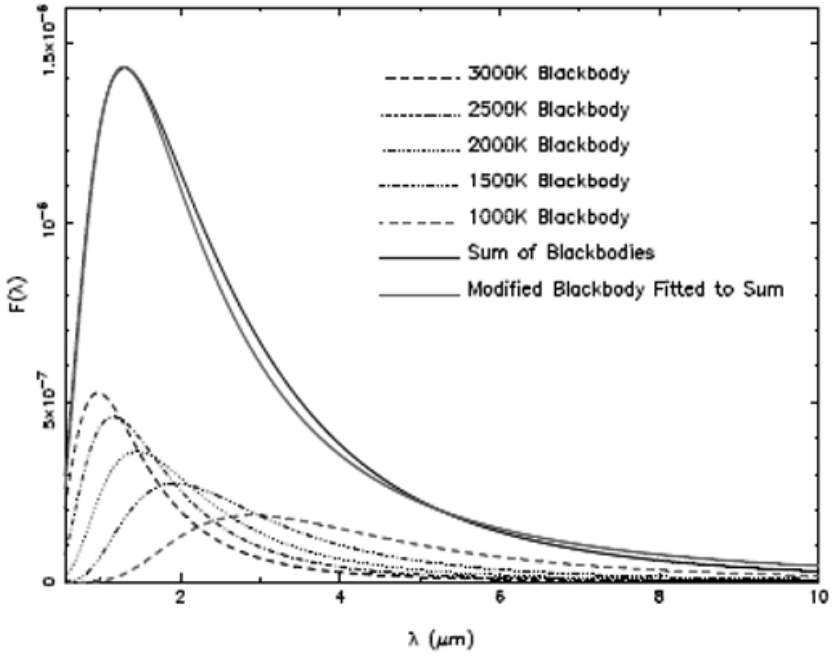

Figure 5.7: A demonstration of the effect of summing blackbodies on the continuum-fitting process. x-axis is wavelength in μm; y-axis is flux density in arbitrary units.

Once we have removed the stellar contribution from the spectrum (i.e., generated F_{dust}), we then fit another blackbody to account for the temperature-dependent dust continuum. There are several ways to conceptualize the dust "continuum". It could be the blackbody ($B_\lambda(T)$) from Equation 5.4, in which case, division by said blackbody would yield the emission efficiency factor Q_λ for a composite dust species including contributions from all dust grains of various sizes and assuming a single temperature. Alternatively, the continuum could be due to a collection of dust grains that contribute to

the overall continuum but do not display diagnostic spectral features (e.g., metallic iron). In this case, the continuum would be one of the C_j x Q_j x B_i components in Equation 5.3, and thus subtracting the continuum to isolate the dust with spectral features is appropriate. Note that in this case we are still left with another C_j x Q_j x B_i component and this residual spectrum is still temperature dependent.

To test the effect of different dust continua, we created blackbodies of 1000 K, 1500 K, and 2050 K for removal. The fits of these continuum blackbodies to the total dust spectrum is shown in Figure 5.4. The conventional (most common) choice for the dust continuum temperature is based on the identification of the 10μm feature as amorphous or glassy silicate. Approximately 1000 K is the typical silicate glass transition temperature (see Speck et al. 2011). Above the glass transition, the silicate grains will either form directly as crystalline material or an amorphous solid will begin to crystallize. The other temperatures we chose coincide with (1) the condensation temperature for olivine and pyroxene, 1500 K; and (2) best fit to the total dust spectrum, F_{dust} without any theoretical considerations about dust stability, 2050 K. While 2050 K is above the stability temperature for any silicates, it is not an unfeasible temperature for the first solids to form (e.g., high temperature oxides, aluminates, or titanates; McSween 1989; Ebel 2006). Furthermore, there is a molecular layer in the atmosphere of Mira with a temperature of 1500–2100 K (Perrin 2004). In addition, this 2050 K blackbody was the best fit for the total dust spectrum and thus serves to test (a) the sensitivity to getting the best fitting continuum rather than using a physically expected value and (b) the effect of temperature on the resulting spectral feature parameters.

Assuming that most of the dust is silicate and that the dust emission can be modeled according to Equation 5.4, we need to divide by the dust-continuum temperature to extract the temperature-independent parameters (Q-values) of the dust spectral features.

As with the measurement of the spectral feature parameters in the total dust spectrum (F_{dust}), we wanted to test for the effect of varying the *star* temperature used to generate F_{dust} prior to dividing out the dust continuum, i.e., we want to know whether there are downstream effects on the spectral feature parameters that depend on early steps in the pathway to continuum elimination. After dividing out the dust continuum, the peak position of silicate spectral features at ~10μm and ~18μm remain unchanged for all stellar temperatures greater than 2493 K, well within the known temperature of Mira for the observation date.

In addition, $F_{dust}/(BB/\lambda^{\beta})$ uses emissivity after subtracting the star. A new blackbody is constructed using dust temperatures of 1000, 1500 and 2050 K, as described above, normalized at 7μm. Each blackbody was modified by an emissivity law; the emissivity index, β, was varied until the best fit (by eye, using the methodology described above) was achieved. This gave β = -0.9, which works for all temperatures above 411 K. The resulting spectra are shown in Figure 5.8 (top row). A range of β values was tested to determine its effect on spectral feature parameters. The peak positions remain unchanged for $-.74 \leq \beta \leq -1.96$. The position and shape of the spectral features is not very sensitive to the temperature or value of emissivity index.

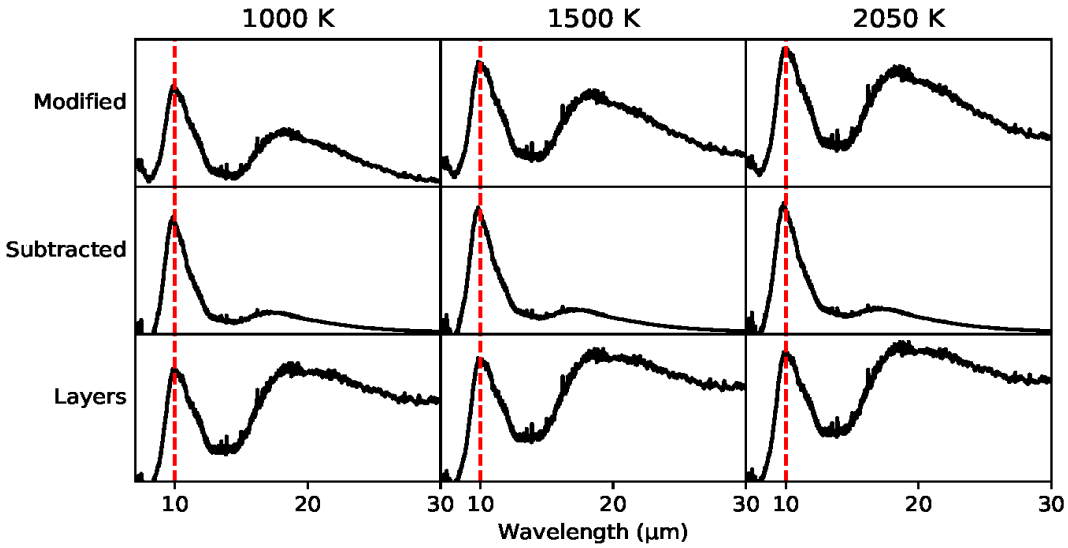

Figure 5.8: The effect of different dust continuum elimination. Each column shows the temperature labeled at the top for the blackbody used for continuum removal. The top row uses a modified blackbody and is the total dust spectrum divided by the blackbody dust continuum for that column, i.e., $F_{dust}/(BB/\lambda^{\beta})$; the middle row shows the total dust spectrum with the dust continuum blackbody subtracted, i.e. F_{dust}-BB_{dust1}; and the bottom row is the same as the middle row, but with a 600 K blackbody divided out. i.e., (F_{dust}-BB_{dust1})/BB_{dust2}.

It is possible that the blackbody fitted to the star-subtracted spectrum (F_{dust}) represents a different dust component than silicate (for example, metallic iron or some form of high temperature oxide). In that case, it is necessary to subtract the dust blackbody to isolate the emission from silicate. Then we need to fit a new blackbody to account for the temperature of the silicate dust. Figure 5.8 (middle row) shows this F_{dust}-BB_{dust1}, with the dust blackbody curve subtracted from the original F_{dust}. The spectral features at ~10μm and ~18μm in the F_{dust}-BB_{dust1} (dust continuum subtracted spectrum) have peaks positions remain the same for a dust temperature range of 1000–3200 K.

The final step is to determine the intrinsic spectral parameters for the silicate features in this 2-dust component scenario. Since this leaves a residual spectrum that is still temperature-dependent, we then fit a second blackbody curve for a dust layer at 600 K, which was divided out to give us the temperature-independent Q-values, i.e. (F_{dust}-BB_{dust1})/BB_{dust2}, shown in Figure 5.8 (bottom row). The ~10μm peak is unchanged for the second dust layer having temperatures ranging 203—663 K, and the ~18μm peak is unchanged for temperatures above 225 K.

5.5. Measurement Results

The results of the spectral feature measurements described in §5.4 are summarized in Table 5.2. I have tested the effect on spectral parameters of using different temperatures and emissivity indices and found that the measurements are not very sensitive to either temperature or emissivity index. However, Table 5.2 shows that the precise pathway to continuum elimination can have a large impact on the peak position, barycenter, and FWHM of the spectral features.

For the ~10μm feature, the peak position is consistent for all pathways to continuum eliminations that start with subtraction of the stellar blackbody, whereas the ~18μm feature is more sensitive to the next steps in the continuum elimination. For the pathways to continuum elimination that do not start with subtracting the star, even the ~10μm feature varies. The barycentric positions for both the ~10μm and ~18μm features show similar trends with the ~18μm peak position, showing that division by a continuum has a major effect on how we measure the position of the silicate features. The implications of these results are discussed in §5.6.

5.6. Discussion

I have investigated the peaks of the ~10μm and ~18μm spectral features using different analysis methods.

We identify dust components in circumstellar spectra by comparing with laboratory data. The precise composition and structure of a silicate will affect the parameters of the ~10μm and ~18μm of spectral features. Comparing the laboratory data parameters from Speck et al. (2011), shown in Table 5.3 and Figures 5.9 and 5.10, and the peak positions and barycenters extracted from the Mira spectrum (shown in Table 5.2), we can see that incorrect continuum elimination will lead to incorrect attributions of minerals to circumstellar features.

For instance, the ~10μm feature peaks at 9.8-9.9μm for both Enstatite and "Cosmic Silicate"[3], but their ~18μm features peak at 17.6μm and 18.3μm, respectively. This means that F_{tot} and F_{dust} are consistent with Enstatite, but $F_{dust}/(BB/\lambda^{\beta})$ and $(F_{dust}-BB_{dust1})/BB_{dust2}$ are consistent with "Cosmic Silicate". Meanwhile, the continuum-elimination pathways that do not subtract the star would suggest a match to Forsterite or Gehlenite.

3 Speck et al. (2011) produces infrared spectra of a silicate glass for which the ratios of the major cations (Mg, Si, Al, Na, Ti) were the same as those of chondrites/the solar system at large but excluded iron. This glass sample was then used to produce the complex refractive index for Cosmic Silicate, where the same sample was measure spectroscopically from 0.2μm to 200μm (Speck et al. 2015).

Table 5.3: Spectral Parameters of Glasses from Speck et al. (2011) (all units are μm)

Sample Name	Peak		Barycenter		FWHM
	~10μm	~18μm	~10μm	~18μm	~10μm
Gehlenite	10.3		10.8		2.86
Akermanite	10.3		10.6		2.46
Forsterite	10.2		10.4		2.43
Diopside	10.1	19.2	10.2	19.4	2.46
Basalt	10.0		9.9		2.41
Enstatite	9.9	17.6	9.9	18.5	2.58
Cosmic Silicate	9.8	18.3	9.7	18.7	3.15
Obsidian	9.0		9.1		2.14
Herasil (SiO2)	9.0		8.9		1.34

When we focus on the barycentric position of the features (rather than peak position), we see similar trends with the ~18μm peak position. The barycentric position of both silicate features is shifted whenever a continuum division is involved in the process of continuum elimination.

Comparing the measured barycenters to those for laboratory samples listed in Table 5.3, we see that the ~10μm feature matches diopside ($CaMgSiO_4$) most closely when there is no continuum division in the elimination pathway but is closer to forsterite for continuum elimination that uses a divided continuum. Unfortunately, we do not have a measurement of the ~18μm feature for this forsterite glass, but the diopside ~18μm feature occurs at a significantly longer wavelength than that observed for Mira in any version of the continuum elimination.

The comparison of both the peak position AND the barycenter position of the dust spectral features is critical to identifying their mineral carriers. Simply measuring the peak position will not suffice.

In addition to the peak and barycentric positions of the observed spectral features, I also measured the FWHM of the ~10μm feature. It is clear from the list in Table 5.2 that the FWHM is quite sensitive to the choice of continuum elimination pathway. Unlike the peak position and barycenter, the FWHM is sensitive to the choice of continuum temperature, making the parameter difficult to use to identify potential mineral carriers.

We need to compare like with like, i.e., ensure that what we take from laboratory data is equivalent to observational data to which we compare. This is discussed extensively in Speck (2013). Figure 5.10 shows the Q_λ values for a range of silicate glass compositions, while Figure 5.9 shows the wavelength dependent absorbance for the silicate glasses for which Speck et al. (2011) measured the ~18μm feature. Absorbance is closer to an optical depth than a Q-value.

Looking back at §5.2.1, we can see for a fairly optically thin dust shell like that of Mira, we should subtract the stellar continuum (see Equation 5.2). This leaves us with a temperature-dependent dust spectrum as given in Equation 5.4. To extract the emission/absorption efficiency, we must divide the observed spectrum by the blackbody temperature of the dust. Without dividing by the dust continuum AFTER subtraction of the star, we should not compare to the Q-values.

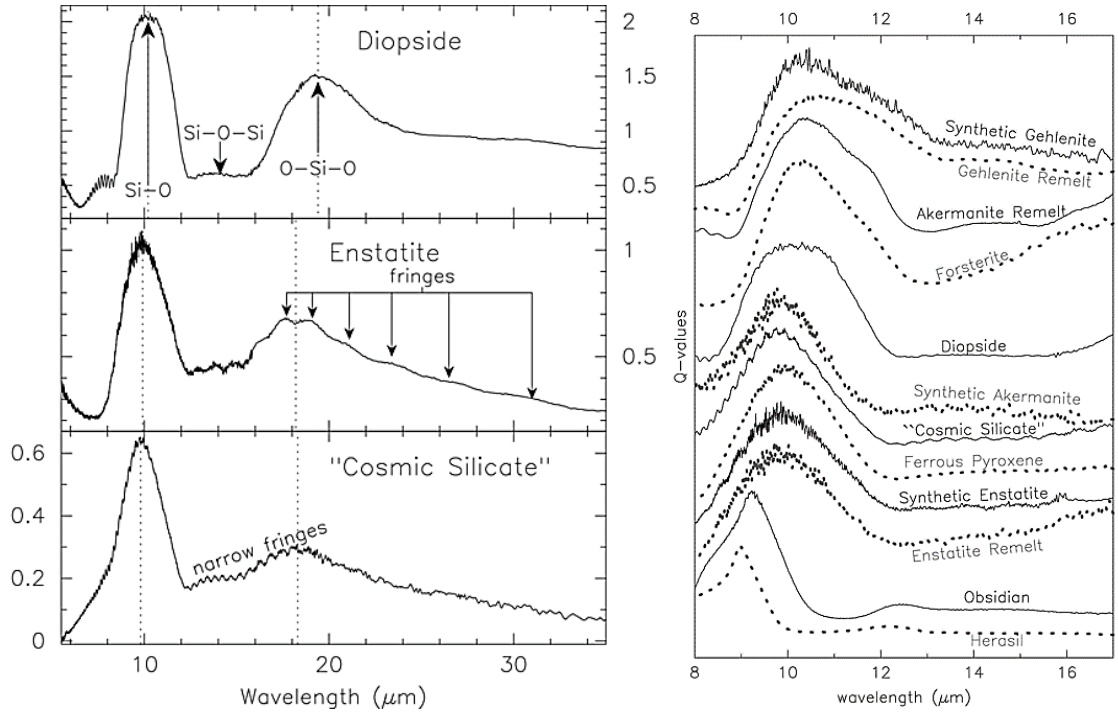

Figure 5.9 (left): Laboratory absorbance spectra for samples from Speck et al. (2011). In all cases the x-axis is the wavelength in μm and the y-axis is absorbance. The dotted line indicates the barycentric positions for the ~10μm and ~18μm features. The wavelengths of the peak positions are listed in Table 5.3.

Figure 5.10 (right): Calculated Q-values (absorption efficiency factors) for samples from Speck et al. (2011). These Q-value spectra are stacked to demonstrate the shift in wavelength of the peak of the ~10μm with composition.

Many of the studies of silicate features in circumstellar dusts, like those mentioned in §5.2.2, simply subtract the stellar continuum and do not completely eliminate the dust continuum. Thus, those spectra cannot be used to infer the mineralogy of the dust.

If we follow any of the continuum elimination pathways that use both stellar continuum subtraction and dust continuum division, we find that for Mira the peak positions of the silicate features are consistently at 9.83 and 18.20μm, while the barycenters occur at 10.4 and 18.9μm (with a little more variability than the peak position). The peak position is consistent with "Cosmic Silicate" while the barycentric position is not. This may suggest the need for a non-silicate component (e.g., alumina; Speck et al. 2000), even in this archetypal strong silicate feature.

It is clear from this study that care must be taken when deconstructing observational spectroscopic data. While radiative transfer modeling may be able to provide a more accurate representation of the temperatures of dust involved in the emission of photons at each wavelength, RT modeling is hampered by a lack of applicable laboratory data. Most radiative transfer modeling uses synthetic complex refractive indices (or dielectric constants) such as Draine & Lee (1984); Ossenkopf, Henning, & Mathis (1992). However, these optical constants are not based on real mineral samples and cannot allow us to extract mineralogical information from observed spectra (see Speck et al. 2015, and references therein). Moreover, there are problems with many of the published refractive indices that are based on real mineral samples (Speck et al. 2011). Consequently, it is difficult to use RT modeling when the goal is to extract the detailed dust mineralogy.

Here I have shown that for low optical depth systems, we MUST subtract a stellar continuum from the observed total spectrum (see Equation 5.1), but the precise T_* value is not critical. Then we must divide by a dust continuum in order to get a spectrum equivalent to the emission efficiency Q_λ (i.e., applying Equation 5.4). In this case we

generate $F_{dust}/(BB/\lambda^{\beta})$ and include the step of subtracting a featureless continuum due to e.g., metallic iron will not change the relevant parameters of the silicate features (although the overall feature-to-continuum ratio may be affected). Failure to subtract a stellar continuum OR divide by a dust continuum will lead to incorrect feature parameters and thus to misidentified astrominerals. As optical depth increases, the application of this simplified deconstruction method becomes problematic and RT modeling becomes necessary. However, at very high optical depth, there are several examples of systems where the continuum can be fitted by a single blackbody (e.g., Speck et al. 2008, 2009). In this case we are observing an isothermal layer in the dust shell outside of which, the dust is optically thin. We usually apply Equation 5.4 to determine the Q_{λ} values for the absorbing dust in the optically thin outer layers, but further study should be undertaken to determine what affect this has, versus treating the isothermal layer as the central "stellar" source.

5.7. Conclusions

I find that for optically thin dust shells, it is possible to deconstruct their spectra to extract detailed mineralogical information. However, the precise pathway by which continua are eliminated has significant effects on the residual dust spectrum and may lead to misidentification of dust species in space. For moderate to high optical depth systems, we cannot apply this simple deconvolution and must apply RT modeling. Unfortunately, RT modeling is hampered by a paucity of complex refractive indices for detailed mineralogical studies. To continue investigating dust in space we need to (a) acquire optical constants (complex refractive indices) of more real mineral samples; and (b)

revisit the many studies of optically thin systems that have classified the silicate features with a new eye to understanding the detailed mineralogy.

Finally, this study suggests that the archetypal/classic silicate feature exhibited by Mira is not consistent with a real amorphous silicate alone but may be best explained with a small alumina contribution to match the observed FWHM of the ~10μm feature.

Chapter 6: Circumstellar Dust around Oxygen-Rich Mira Variables with Maser Emission

6.1. Introduction

This project investigates the formation of circumstellar dust by using a sample of oxygen-rich Mira variables for which maser emission has been identified. Using high-resolution spectroscopy data along with ancillary data from the published literature, I explored a relationship between the presence of maser emission and dust spectral features for the sample of Mira variables. I have investigated the continuum-eliminated spectra by first matching the positions and widths of observed spectral features with those seen in laboratory spectra and then determining whether trends exist between the maser emission and dust spectral features.

6.2. Connecting Masers and Circumstellar Dust

There are very few studies that explore the possible connection between maser emission and circumstellar dust around AGB stars. Those that do exist primarily look at overall statistics between AGB stars and the presence of a certain maser species. Sobolev et al. (2019) examined a sample of 1803 known long-period variable (LPV) objects and found that 46% of these stars manifest maser emission in the line of at least one molecule of H_2O, OH, or SiO. Lewis (1996) documented the low-resolution spectral type (LRS) dependence on the frequencies of H_2O, OH, and SiO masers detected from circumstellar shells. He found that 67% of shells with silicate emission features and 27% of those without have main line OH masers (1665 Hz and 1667 Hz) when they also have a known water or SiO maser. Simultaneous observations have been made of both SiO and H_2O

masers (Kim et al. 2010) towards 166 known SiO and H_2O maser sources. The sources consisted of 101 Mira variables, 13 OH/IR stars, 15 semi-regular variables, 7 supergiants, and the remainder were unidentified objects. Both types of maser emission were detected from 112 sources, giving a detection rate of 67% during each period of observation. SiO-only maser emission was detected from 42 sources, while H_2O-only maser emission was detected from 4 sources. This study focused on maser data and not dust.

Little-Marenin & Little (1990) used a sample of 291 Mira variables to check for correlations with different classes of dust grain features and the percentage of Mira variables that have maser detection in the SiO, H_2O, and OH molecules. The classes of dust grain features include Sil (characteristic silicate emission feature with a maximum at 9.8μm), Sil+ (characteristic silicate emission with a maximum at 9.8μm, but with a bump developing on either side of the silicate feature at ~11.3μm), and Sil ++ (the bump at 11.3μm is becoming nearly as prominent as the 9.8μm feature). They found that maser emission from OH and H_2O is much more frequently detected in stars that show the Sil or Sil+ emission feature, but SiO maser emission is detected with the same percentage (~60%) in all silicate emission feature classes. Roughly 60% of the Miras with Sil and Sil+ features have all three (SiO, H_2O, and OH) masers. The percentage associated with H_2O and OH masers decreases to about 20% for Miras with Sil ++ (SiO maser detection remains at ~60%).

Since maser emission is associated with energy and density of molecules around a star, it is expected that the presence of a maser is related to what type of dust forms. An analysis employing radiative transfer code on a sample of IRAS AGB sources exhibiting 1612 MHz OH masers (Faesi & Lewis 2010) showed that the temperature of the hottest

dust in the circumstellar shell is much cooler in objects without masers, which suggests that their dust shells have a different dust composition. The studies presented in that work indicate that it is worthwhile to look for further connections between the presence of a maser and dust spectral features.

6.3. Sample

When looking for correlations between parameters, it is important to have a statistically significant sample of stars. To that end, the first step is to have a sample of stars for which there is both maser emission and high-resolution space-based spectroscopy data. The Sloan Spectral Atlas (accessed at https://users.physics.unc.edu/~gcsloan/library/swsatlas/aot1.html) includes entries for all 1239 full-scan AOT1 spectra from the Infrared Space Observatory (ISO; Kessler et al. 1996) Short Wavelength Spectrometer (SWS; de Graauw et al. 1996), processed as explained by Sloan et al. (2003). From this list, there are 800+ unique objects with valid SWS full-scan 2.4-45.4 μm spectra, processed and renormalized in as uniform a manner as possible. The processing produces a single spectrum for each observation from the 288 individual spectral segments, which are the most processed form available from the ISO archive. The sample used for this project was determined by cross-referencing the list of 800+ stars with information about whether maser emission occurs. This was achieved using a search thru archives (e.g., the SAO/NASA Astrophysics Data System; (ADS; accessed at http://adsabs.harvard.edu/abstract_service.html) to find maser emission data for each object. 500+ objects have been identified as having SiO, H_2O, or OH masers. Many have more than one type of maser.

The next step was to determine which of these sources would be good for analysis. We want oxygen-rich evolved stars which have both fully processed spectra and maser emission data for each type of maser. This project focuses on optically thin Mira variables having silicate emission. There were 33 Mira variables having 2.SE spectral class in the Sloan Spectral Atlas, indicating the sources are objects with a silicate or oxygen-rich dust emission feature at 10-12μm, usually accompanied by a secondary feature at 18-20μm. Table 6.1 lists these sources along with the IR spectral class and what types of masers have been detected with the source, if any.

SED data for each star in the form of photometric measurements of brightnesses/magnitudes in different colors is obtained from the SIMBAD archive of astronomical data. Here we find spectral type, used to constrain the model star temperature, as well as magnitudes for UBVJHK bands. SIMBAD also gives IRAS photometric fluxes at 12, 25, 60, and 100 microns in Janskys. All this data put together was plotted and used to constrain the models. Each variable star has a range of spectral types, and these correspond to a range in stellar temperatures. Checking the date of ISO SWS observation against the AAVSO light curve (if available) for a star allows for a good approximation of a star's temperature at the time of observation.

Source	IR class	SiO	H2O	OH	NONE	Spectral Class	Temperature
O Cet (Mira)	2.SEc	✓	✓			M5-9IIIe	3420
AFGL 3022	2.SEc	✓				M6	2600
BU And	2.SEa	✓	✓			M7e	2600
GY Aql	2.SEc	✓		✓		M6IIIe-M8	2400
IRC +00490	2.SEc	✓				M7, M8	2350
IRC -30023	2.SEc	✓	✓			M7-M9	2450
R Cas	2.SEb	✓	✓	✓		M6e-M10e	2600
R Cen	2.SEap	✓				M4e-M8IIe	3000
R Hya	2.SEa	✓	✓			M6-9e	2600
R Peg	2.SEa	✓	✓			M6-8.5e	2600
RR Aql	2.SEc	✓	✓	✓		M6e-M9	2700
RR Per	2.Sea	✓	✓	✓		M6e-M7e	2750
RS Lib	2.SEa:	✓				M7e-M8.5e	2550
RU Phe	2.SEc:				✓	M1e	3450
RX Vul	2.SEa	✓				M9	2450
RY And	2.SEa:	✓	✓			M8	2300
S Lac	2.SEa				✓	M4e-M8.2e	3000
S Pav	2.SEa	✓				M7IIe-M8III	2500
S Scl	2.SEb	✓	✓			M3e-M9e	2900
S Vir	2.SEa	✓	✓			M6IIIe-M9.5e	2700
SS Peg	2.SEa	✓				M6e-M7e	2750
SV And	2.SEa	✓				M5-7e	2900
T Cas	2.SEa	✓				M6e-M9.0e	2600
T Cep	2.SEa	✓				M5.5e-M8.8e	2800
TW Cyg	2.SEa	✓				M6.5-M10e	2700
TX Cam	2.SEc	✓	✓			M8-M10	2650
U Her	2.SEc	✓	✓	✓		M6.5e-M9.5e	2700
U Tel	2.SEc	✓				M7e	2700
UX Cyg	2.SEc	✓	✓	✓		M4e-M6.5e	2800
W Hya	2.SEa	✓	✓	✓		M7.5-9e	2700
X Oph	2.SEa	✓	✓	✓		M5e-M9e	2650
Z Cas	2.SEap	✓				M7e	2750
Z Cyg	2.SEc	✓	✓	✓		M5e-M9e	2850

Table 6.1: Sample Data. The star name, the IR class as classified by Sloan et al. (2003), types of masers that have been identified, observation date, and stellar temperature used. "2.SE" indicates the source has silicate (or oxygen-rich) dust emission in 10-12μm and 18-20μm. The lowercase letters indicate the presence of one or more spectral features:

“a” broad emission feature peaking at 12.1μm, “b” 10.1 dust feature due to amorphous silicates and a secondary peak at 11.1μm, “c” strong silicate emission features with peaks at 10 and 18.1μm. In addition, “p” signifies that the spectrum fits in that category but is peculiar, and “:” indicates a noisy or odd spectrum. The spectral type column gives the range reported by SIMBAD; and the temperature column gives the effective temperature of the star used for modeling.

All 33 Mira stars were analyzed using a continuum-fitting method as described in §5.4. The approximated temperature of each star was used to subtract a stellar blackbody from the total flux to obtain a dust-only spectrum. The next step was to fit the dust continuum with a modified blackbody of the form $BN = B\lambda^{-\beta}$, where β is the emissivity index for the dust. Results from the previous chapter show the spectral feature measurements are not very sensitive to either temperature or emissivity index, and the peak positions were the same for fitting a modified blackbody to the continuum compared to removing the continuum in layers.

The peak positions near 10μm and 18μm were also measured. The results of these spectral feature measurements along with notes about each spectrum are reported in Table 6.2. From the sample of 33 Mira variables, 12 had clear enough spectra for further analysis. The rejected stars had spectra which either was too noisy to analyze or lacked peaks to be examined, as described in Table 6.2. Figure 6.1 shows the spectra after a modified blackbody is fit to the dust-only continuum. The barycentric positions of the 10μm and 18μm features as well as the FWHM for the 10μm feature were measured and are listed in Tables 6.3 and 6.4. The 18 μm features are not consistently defined, and FWHM values are not reported.

Table 6.2: The measured peak positions near 10μm and 18μm are listed for each star. Notes are shown detailing the usability of each spectrum for analysis. From this sample of 33 stars, 12 had clear enough peaks for further analysis.

Source	peak ~10μm	peak ~18μm	Notes
O Cet	9.83	18.20	Very clear peaks for both
AFGL 3022	10.09	17.77	Clear peaks but noisy at higher wavelengths
BU And	10.50	18.38	Does not peak in that region, appears shifted
GY Aql	10.06	18.50	Very clear peaks, 10 is high
IRC +00490	9.75	18.39	10 is very clear and high, 18 is good
IRC -30023	10.04	18.41	Very clear peaks, 10 is high
R Cas	10.48	17.89	Clear peak, 10 looks like it also peaks lower
R Cen	10.48	18.27	Appears double-peaked about the same height
R Hya	10.48	18.41	10 is fuzzy, 18 is clear
R Peg	10.47	17.78	Not clear
RR Aql	9.84	18.01	Very clear peaks, 10 is high
RR Per	10.48	17.91	Not clear
RS Lib	9.71	18.26	Not clear at all
RU Phe	10.34	18.31	Not clear, peaks near 10, 18 is too fuzzy
RX Vul	10.16	17.99	Does not peak in that region, 10 appears shifted, 18 not clear at all
RY And	9.85	17.58	No clear peaks, continues to climb
S Lac	10.21	17.72	No clear peaks
S Pav	10.50	17.99	No clear peaks
S Scl	10.50	18.49	No clear peaks
S Vir	10.15	18.29	No clear peaks
SS Peg	10.44	17.79	No clear peaks, decreases at higher wavelengths
SV And	10.08	17.71	No peaks
T Cas	10.48	18.39	No clear peaks
T Cep	10.48	18.00	Does not peak in that region, appears shifted
TW Cyg	10.46	17.52	No clear peaks, very noisy
TX Cam	10.31	18.28	10 is very clear, 18 is not
U Her	10.19	18.49	Clear peaks, 10 is higher
U Tel	10.10	18.20	10 is very clear, 18 is there but fuzzy
UX Cyg	9.82	18.40	10 is very clear, 18 is good
W Hya	10.48	18.00	No clear peaks
X Oph	10.45	18.00	No clear peaks
Z Cas	10.40	18.43	Not clear, 10 peak is shifted higher
Z Cyg	9.87	18.37	10 is very clear, 18 is extended very wide to higher wavelengths

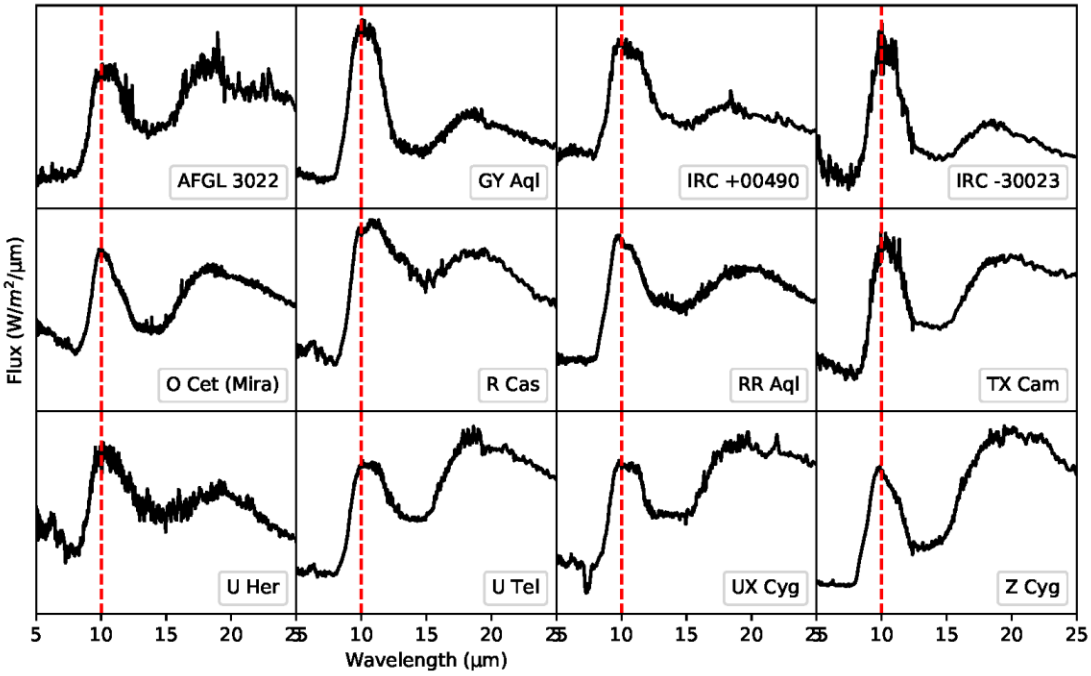

Figure 6.1: The dust spectrum of the 12 Mira variables after fitting with a modified blackbody. The x-axis is the wavelength in μm; y-axis is flux density in $Wm^{-2}\mu m^{-1}$.

Table 6.3: Peak position, barycentric position, and FWHM of the ~10μm feature. Stars are sorted in order of increasing barycenter.

Star	~10μm Peak (μm)	Barycenter (μm)	FWHM (μm)
Z Cyg	9.87	10.13	2.72
RR Aql	9.84	10.20	3.02
UX Cyg	9.82	10.29	2.68
GY Aql	10.06	10.32	2.76
IRC -30023	10.04	10.35	2.39
TX Cam	10.31	10.39	2.74
U Tel	10.10	10.39	2.95
Mira (O Cet)	9.83	10.39	2.54
IRC +00490	10.36	10.39	3.08
AFGL 3022	10.09	10.40	2.42
R Cas	10.48	10.41	3.44
U Her	10.19	10.42	3.33

Table 6.4: Peak position and barycentric position of the ~18μm feature. Stars are sorted in order of increasing barycenter.

Star	~18μm Peak (μm)	Barycenter (μm)
AFGL 3022	17.77	18.72
Mira (O Cet)	18.20	18.88
IRC +00490	18.39	18.96
GY Aql	18.50	18.98
TX Cam	18.28	19.06
IRC -30023	18.41	19.09
U Tel	18.20	19.10
Z Cyg	18.37	19.15
R Cas	17.89	19.23
UX Cyg	18.40	19.23
RR Aql	18.01	19.34
U Her	18.49	19.38

6.4. Measurement Results

The results of the spectral feature measurements described in §6.3 are summarized in Tables 6.3 and 6.4. I have examined a sample of Mira variables having maser emission and identified 12 stars with clear enough spectra for analysis. Having measured the peak and barycentric positions of both the 10 and 18μm features as well as the FWHM of the 10μm feature, I sought correlations between these measurements and with the presence of the various maser emissions. This was achieved by applying least-squares fits to the data; a correlation was deemed significant for a determination coefficient (R^2) greater than 0.5 (see Messenger, Speck & Volk 2013). Interestingly, we did not find ANY correlations between the spectral feature parameters (i.e., peak and barycentric positions of both the 10 and 18μm features and the FWHM).

In the search for correlations between the presence of any combination SiO, H_2O, or OH maser and the spectral feature parameters, there appears to be no relation save for one: the number of maser types and the position of the ~18μm barycenter. Figure 6.2 shows that the R^2 value (coefficient of determination) is 0.6057. All other pairs of parameters had $R^2 << 0.5$. The implications of a lack of relationships between measured values are discussed in §6.5.

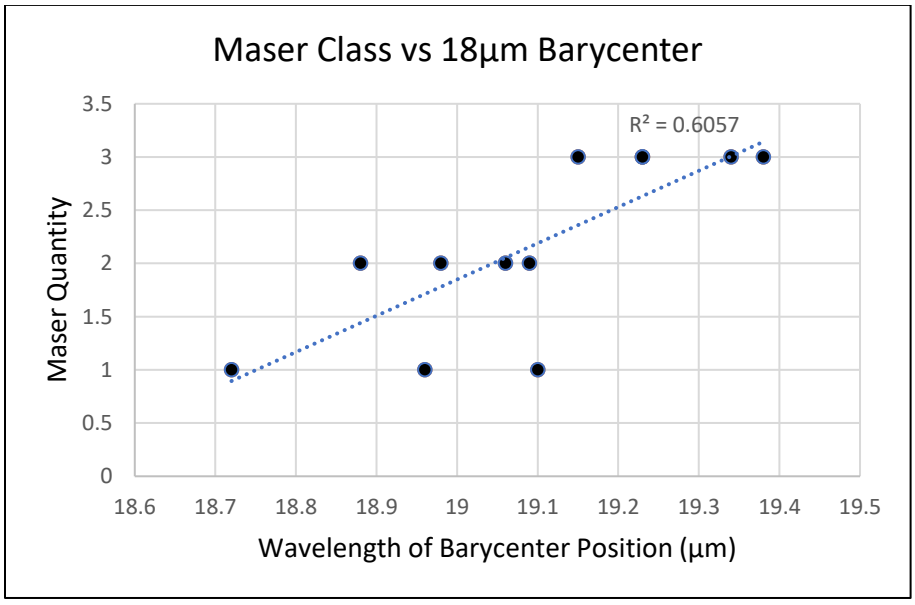

Figure 6.2: The number of masers versus the wavelength of the ~18μm barycenter

6.5. Discussion

I have looked for a correlation between maser emission and dust spectral features in a sample of Mira variables. The types of masers have been identified, and peak positions, barycentric positions, and FWHM have been measured for the sample spectra.

Similar to the method used in the previous chapter, the first step in identifying the nature of dust grains in space is to match the positions and widths of observed spectral features

with those seen in laboratory spectra. Comparing the laboratory data parameters from Speck et al. (2011), shown in Table 5.3 in the previous chapter, to the measurements in reported in Tables 6.3 and 6.4, we see that the most consistent values are in the barycenter position near 10μm and correspond to a composition of Forsterite. The 18μm feature has groupings of similar barycenter position, but we do not have corresponding lab data at these values. We do not have lab measurements for Forsterite or many other compositions for the 18μm feature to use for comparison. A couple stars have features that are consistent with Diopside when considering both 10μm and 18μm features.

The inconsistent values in the peak positions may be due to the noise in some of the spectra, and the barycenter position will give the more weighted measurement. It is worth noting that the two stars with the most noise seen in their spectra, AFGL 3022 and U Her, are on the boundaries of the measurements for the 18μm barycenter.

The lack of any correlations between the spectral features suggest that we need to use different combinations of minerals for each star. As seen in the previous chapter, the comparison of the peak and barycentric position and FWHM suggest that silicates alone cannot explain the features. The complexity of the spectral features indicates complex silicate compositions, and that means the one correlation (that of the 18μm barycenter and number of maser types) is meaningless.

The spectral data acquired from ISO has longer wavelengths than the available laboratory data used for spectral feature comparison. Since less lab data is available for the 18μm feature than the 10μm feature, more lab data would be useful to aid in mineral identification. The combination of peak and barycenter position at both 10μm and 18μm

can be a powerful tool for mineral identification, but we are limited by the data available at this time.

The lack of a correlation between maser species and spectral features may be due to the difficulty in measuring the strength of a maser. These stars are variable, and the masers surrounding them are also variable. We do not have data for maser strength at the time of observation. A study monitoring 22 Mira and semi-regular variables over many pulsation cycles (Benson et al. 1993) found the intensity of H_2O masers to vary markedly. SiO masers exhibit similar changes in intensity (Bujarrabal et al. 1993). Extensive statistical data on H_2O maser variability around Mira variables (Rudnitskij 2002) suggests that there are two groups of circumstellar H_2O masers: (1) "Stable" masers which displayed H2O emission throughout several years of observation without falling below the detection threshold (~10 Jy). The masers still have varying intensity. (2) "Transient" masers which sometimes disappeared from view and fell below the detection threshold for some intervals, sometimes for more than 15 years. Chen et al. (2001) found while assembling their database of OH 1612 Hz maser emission that the data is rather non-uniform: the different OH maser surveys have different detection thresholds and vary from inaccurate radio positions for the single-dish surveys to highly accurate radio positions for the interferometric surveys. There is information available about maser angular diameter, peak flux, peak velocity, and transition lines; these qualities can be used to continue looking for correlations.

6.6. Conclusions

From this study, I conclude that there is no obvious correlation between the presence of a maser emission and dust spectral features. Previous studies suggest that

there should be some relationship between circumstellar dust and the presence of a maser. The lack of any correlations between the spectral features suggest that we need to use different combinations of minerals for each star. This needs to be investigated further with a larger sample of stars, and if possible, more quantitative data about maser emission for each star. Future work to be done in this area is described in the next chapter.

Chapter 7: Conclusions and Future Work

7.1. Summary and Conclusions

In the preceding work, I have investigated several methods of continuum elimination using spectroscopy data for the archetypal dusty AGB star, Mira. I have investigated the ~10μm and ~18μm spectral features in the continuum-eliminated spectrum including peak position, barycenter, and FWHM. The positions and widths of observed spectral features were compared with those seen in laboratory spectra. I then looked for a correlation between maser emission and dust spectral features in sample of Mira variables. The types of masers have been identified, and peak positions, barycenter positions, and FWHM have been measured for the sample spectra. The conclusions of these studies are as follows.

7.1.1. Continuum Elimination

The precise pathway by which continua are eliminated has significant effects on the residual dust spectrum and may lead to misidentification of dust species in space. While the precise continuum shapes and temperatures do not have a critical impact on interpreting dust spectral features, it is important to eliminate continua in a specific way. To continue investigating dust in space, we need to acquire more optical constants of more real mineral samples. This study suggests that the archetypal/classic silicate feature exhibited by Mira is not consistent with a real amorphous silicate alone but may best be explained with a small alumina contribution.

7.1.2. Circumstellar Dust and Maser Emission

There does not appear to be any correlation between the presence of a maser and dust spectral features. This could be due to the small sample size, or it could be due to a lack of quantitative data about the masers at the time of observation. Previous studies indicate that there should be a relationship. Silicate features are difficult to interpret and indicate complex compositions. The lack of any correlations between the spectral feature parameters suggest that we need to use different combinations of minerals for each star.

7.2 Future Work

There is an opportunity for further investigation into a relationship between circumstellar dust and maser emission. The availability of maser strength data at different time periods limits the work that can be done in that direction. There is information about maser angular diameter, peak flux, peak velocity, and transition lines; these qualities can be compiled into a study looking for correlations. The obvious step is to have a larger sample of stars for comparison. Additional spectra can be obtained from the Infrared Astronomical Satellite (IRAS) low resolution spectrometer (LRS; Vardya et al. 1986), which can be found at http://isc83.astro.unc.edu/iraslrs/getlrs_test.html. Little-Marenin & Little (1990) used IRAS data when checking for correlations with different classes of dust grain features and the percentage of Mira variables that have maser detection. However, my analysis method would differ by applying to each individual spectrum instead of the spectral classes. Variations are subtle in the spectral classes (but can be established), and the larger dataset from IRAS would give better statistics.

The spectrum of each star could also be analyzed using radiative transfer (RT) modeling. Radiative transfer (RT) modeling uses the optical constants (complex refractive indices, n & k) of candidate minerals to model how a given object should look both spectroscopically and in images. RT modeling determines the effects of grain size distributions and mineralogy on the expected spectrum, and places constraints on the relative abundances of grain types in a dust shell. We can utilize the one-dimensional RT code DUSTY (Ivezic & Elitzur 1195; Nenkova et al. 2000) to obtain a match to the overall SED with certain parameters. DUSTY uses optical constants derived from laboratory data to generate spectra given shell size, intrinsic shell thickness, density/optical depth, blackbody temperature, inner dust temperature, composition, grain size, and grain shape.

It is known that different maser species are located in different shells with increasing distance to a star with some stars having more than one type of maser. This information can be used to create multiple-shell models using different dust compositions.

Even if no correlation is found between the presence of a maser and spectral features, the models will still be used to study potential correlations between the chemistry of the star and the circumstellar dust. The information gained may be able to distinguish between different dust formation mechanisms.

REFERENCES

Aitken, R. G. 1923, PASP, 35, 323

Allard, F. 2016, in SF2A-2016: Proceedings of the Annual meeting of the French Society of Astronomy and Astrophysics. Eds.: C. Reylé, J. Richard, L. Cambrésy, M. Deleuil, E. Pécontal, L. Tresse and I. Vauglin, pp.223-227

Baan, W. A., Wood, P. A. D., Haschick, A. D. 1982, ApJ, 260, L49

Barrett, A. H., Swartz, P., R., Water, J. W. 1971, ApJ, 168, L101

Batrla, W., et al. 1987, Nature, 326, 49-51

Benson, P. J., Little-Marenin, I. R. 1996, ApJS, 106, 579

Benson, P. J., Little-Marenin, I. R., Cadmus, R. R. 1993, in Astrophysical Masers, ed. A. W. Clegg & G. E. Nedoluha (Berlin: Springer), 271

Blocker, T. & Schonberner, D. 1991, A&A, 244, L43

Bode, M. F. 1988, in Dust in the Universe, eds. M. E. Baily and D. A. Williams. Cambridge: Cambridge University, 73

Bujarrabal, V., et al. 1993, in Astrophysical Masers, ed. A. W. Clegg & G. E. Nedoluha (Berlin: Springer), 421

Casassus, S., Roche, P. F., Aitken, D. K., Smith, C. H. 2001, MNRAS, 320, 424

Chen, P. S. et al. 2001, A&A. 368, 1006

Cheung, A. C., et al. 1969, Nature, 221, 626

Chiar, J. E., Ennico, K., Pendleton, Y. J., et al. 2007, ApJ, 666, L73

Chigai, T. & Yamamoto, T. 2003, Geochim. Cosmochim. Acta, 67, 64

Claussen, M. J., Frail, D. A., Goss, W. M., Gaume, R. A. 1997, ApJ, 489, 143

Cosmovici, C. B., et al. 1995, BAAS, 412

Davies, R. D., et al. 1967, Nature, 213, 1109-1110

de Graauw, T., et al. 1996, A&A, 315, L49

Demyk, K., Meny, C., Lu, X.-H., et al. A&A, 600, 123

DePew K., Speck A., Dijkstra C. 2006, ApJ, 640, 971

Dijkstra, C., Speck A. K., Reid R. B., Abraham P. 2005, ApJ, 633, L133

Draine, B. T., Lee, H. M. 1984, ApJ, 285, 89

Draine, B. T. 2003, ARA&A, 41, 241

Ebel, D. 2006, in Meteorites and the Early Solar System II, D. S. Lauretta and H. Y. McSween Jr. (eds.), University of Arizona Press, Tucson, 943 pp., p.253-277

Elitzer, M. 1992, Annu. Rev. Astron, Astrophys., 30, 75

Elitzur, M. 1980, ApJ, 240, 553

Faesi, C., Lewis, B. M. 2010, Bulletin of the AAS, 42, 342

Feast, M. W. 1996, MNRAS, 278, 11

Fish, V. L., Reid, M. J., Argon, A. L., Menten, K. M. 2003, ApJ, 506, 328

Gail, H. P. & Sedlmayr, E. 1999, A&A, 347, 594

Garcia-Barreto, J. A., Burke, B. F., Reid, M. J., Moran, J. M., Haschick, A. D., Schilizzi, R. T. 1988, ApJ, 326, 954

Gautschy, A. & Saio, H. 1996, ARA&A, 34, 551

Gillett, F. C., Low, F. J., Stein, W. A. 1968, ApJ, 154, 677

Gray, M. 1999, Phil. Trans. R. Soc. Lond. A (1999) 357, 3277

Gray, M. D., Field, D. 1994, AA, 292, 693-698

Gray, M. 2012, Maser Sources in Astrophysics, Cambridge University Press, Cambridge

Green, A. J., et al. 1997, ApJ, 114, 2058

Grossman, L. 1972, Geochim. Cosmochim. Acta, 36, 597

Habing, H. J. 1996, A&AR, 7, 97

Hackwell, J. A., Gehrz, R. D., and Woolf, N. J. 1970, Nature, 227, 822

Hao, Lei, Spoon, H. W. W., Sloan, G. C., et al. 2005, ApJ, 625, L75

Hofner, S. & Dorfi, E. A. 1997, A&A, 319, 648

Iben, I., Jr. & Renzini, A. 1983, ARA&A, 21, 271

Ivezic, Z. & Elitzur, M. 1995, ApJ, 445, 415

Kessler, M. F., et al. 1996, A&A, 500, 493

Kim, J. et al. 2010, ApJ SS, 188, 209

Knacke, R. F. et al. 1969, ApJ, 155, L189

Knowles, S. H., et al. 1969, Science, 163, 1055

Koike, C., Hasegaqwa, H., Hattori, T. 1987, Ap&SS, 134, 95

Koike, C., Hasegaqwa, H., Manabe, S. 1980, Ap&SS, 67, 495

Kraemer K. E., Sloan G. C., Price S. D., Walker H. J. 2002, ApJS, 140, 389

Krishna-Swamy, K. S., 2005, in Dust in the Universe: Similarities and Differences, World Scientific Series in Astronomy and Astrophysics, Vol. 7. Singapore: World Scientific Publishing, 252

Krugel, E. 2008, An Introduction to the Physics of Interstellar Dust, New York: Taylor & Francis Group, LLC, 387

Kwok, S. 2004, Nature, 430, 985

LeBlanc, F. 2010, An Introduction to Stellar Astrophysics, Wiley, West Sussex

Lewis, B. M. 1996, ApJ, 462, 786

Lewis, B. M. 1998, ApJ, 508, 2, 831

Little-Marenin, I. R., Little S. J. 1988, ApJ, 333, 305

Little-Marenin, I. R., Little S. J. 1990, ApJ, 99, 1173

Lo, K. Y. 2005, ARA&A, 43, 625-676

Lodders, K., & Fegley, B., Jr. 1995, Meteoritics, 30, 661

Lodders, K., & Fegley, B., Jr. 1999, in Asymptotic Giant Branch Stars, eds. T. Le Berte, A. Lebre, and C. Waelkens, IAU Symp. 191, Astron. Soc. Pacific, New York: Springer, 279

Mann, I., Köhler, M., Kimura, H., Cechowski, A., Minato, T. 2006, A&ARev, 13, 159

Markwick-Kemper, F., Gallagher, S. C., Hines, D. C., Bouwman, J. 2007, ApJ, 668, L107

McSween, H. Y., 1989, American Scientist, 77, 146

Mennella, V., Brucato, J. R., Colangeli, L., Palumbo, P., Rotundi, A., Bussoletti, E. 1998, ApJ, 496, 1058

Messenger, S. J., Speck, A., Volk, K. 2013, ApJ, 764, 142

Molster, F. J., Waters, L. B. F. M., Tielens, A. G. G. M., Barlow, M. J. 2002, A&A, 382, 184

Nenkova, M., Ivezic, Z., & Elitzur, M. 2000 in ASP Conf. Ser. 196, Thermal Emission Spectroscopy and Analysis of Dust, Disks, and Regoliths, ed. M. L. Sitko, A. L. Sprague & D. K. Lynch (San Francisco: ASP), 77

Ogley, R. N., et al. 1997, Irish Astr. J, 24, 97

Ossenkopf, V., Henning, Th., & Mathis, J. S. 1992, A&A, 261, 567.

Peeters, E., Hony, S., Van Kerckhoven, C., Tielens, A. G. G. M., Allamandola, L. J., Hudgins, D. M., and Bauschlicher, C. W. 2002, A&A, 390, 1089

Percy, J. R. 2007, Understanding Variable Stars, Cambridge University Press, Cambridge

Perrin, G., Ridgway, S. T., Mennesson, B., et al. 2004, A&A, 426, 279

Pickles A. J. 1998, PASP, 110, 863

Rudnitskij, G. M. 2002, Publ. Astron. Soc. Aust. 19, 499

Samus, N. N., Kazarovets, E. V., Durlevich, O. V., Kireeva, N. N., and Pastukhova, E. N. 2017, Astron. Rep., 61, 80, General Catalogue of Variable Stars: Version GCVS 5.1 (http://www.sai.msu.su/gcvs/gcvs/index.htm)

Seigman, A. E. 1986, Lasers, University Science Books, Sausalito, CA

Sharp, C. M. & Wasserburg, G. J. 1995, Geochim. Cosmochim. Acta, 59, 1633

Sloan, G. C., Kraemer, K. E., Goebel, J. H., Price, S. D. 2003A, ApJ, 594, 483

Sloan, G. C., Kraemer, K. E., Price, S. D., Shipman, R. F. 2003B, ApJS, 147, 379

Sloan, G. C., Price, S. D. 1995, ApJ, 451, 758 Sloan G. C., Price S. D. 1998, ApJS, 119, 141

Sobolev, A. J., Ladeyschikov, D. A., and Nakashima, J. 2019, Res. Astron. Astrophys. 19, 3

Speck, A. K., Barlow, M. J., Sylvester, R. J., Hofmeister, A. M. 2000, A&A, 146, 437

Speck, A. K., Pitman, K. M., Hofmeister, A. M. 2015, ApJ, 809, 65

Speck, A. K., Whittington, A. G., Hofmeister, A. M. 2011, ApJ, 740, 93

Speck, A. K., Whittington, A. G., Tartar, J. B. 2008, ApJ, 687, L91

Speck, A. K. 2009, ApJ, 691, 1202

Speck, A. K., Corman, A. B., Wakeman, K., Wheeler, C.H., Thompson, G. 2009, ApJ, 691, 1202

Speck, A. 2013, in Proceedings of The Life Cycle of Dust in the Universe: Observations, Theory, and Laboratory Experiments, eds. A. Andersen, M. Baes, H. Gomez, C. Kemper, and D. Watson, Taipei, Taiwan, LCDU2013

Strelnitski, V. 1997, Masers, Lasers, and the Interstellar Medium, Astrophysics and Space Science, 252

Sylvester, R. J. et al. 1999, A&A, 352, 587

Synder, L. E. & Buhl, D. 1974, ApJ, 189, L31

Tayler, R.J. 1996, The Stars: their structure and evolution, Cambridge University Press, Cambridge

Tielens, A. G. G. M., et al. 1997, Astrophys. & Space Science 255, 415

Townes, C. H. 1964, Production of coherent radiation by atoms and molecules, Nobel Lecture

Vardya, M. S., et al. 1986, ApJ, 304, L29

Vassiliadis, E. & Wood, P. R. 1993, ApJ, 413, 641

Videen, G., & Kocifaj, M. 2002, Optics of Cosmic Dust: proceedings of a NATO Advanced Research Workshop NATO Science Series. Dordrecht/Boston/London: Kluwer Academic Publishers

Vlemmings, et al. 2006, A&A, 448, 597

Volk, K., & Kwok, S. 1987, ApJ, 315, 654

Volk, K., Xiong, G., & Kwok, S. 2000, ApJ, 530, 408

Watson, C., Henden, A. A., and Price, C. A. 2014, AAVSO International Variable Star Index VSX (https://www.aavso.org/vsx)

Weaver, H., et al. 1965, Nature, 208, 29-31

Weinreb, S., et al. 1965, Nature, 208, 440

Whiteoak, J. B, & Gardner, F. F. 1973, Astrophys. Lett, 15, 211

Wilson, R. W., et al. 1971, ApJ, 167, L97

Wilson, W. J. & Barrett, A. H. 1968, Science, 161, 728

Woitke, P. 2006, A&A, 460, L9

Woolf, N. J. 1973, in Circumstellar Infrared Emission, Interstellar Dust and Related Topics, IAU Symposium No. 52, eds. J. M. Greenberg and H. C. Van de Hulst, Dordrecht: Reidel, 485

Woolf, N. J., and Ney, E. P. 1969, ApJ Lett. 155, L181

VITA

Lisa Shepard grew up in rural southeastern Wisconsin on the Fox River. She became interested in astronomy as a young child when her older brother told her that the Moon was made of cheese. It turns out that was a lie, but Lisa still has a good look at the Moon every time it is visible in the sky. Since then, Lisa has also been relieved to learn that “shooting stars” are not actually stars falling from the sky. Lisa’s level of astronomy knowledge really has come a long way!